

**GLOBULAR CLUSTER PHOTOMETRY WITH
THE HUBBLE SPACE TELESCOPE¹. V.
WFPC2 STUDY OF M15'S CENTRAL DENSITY CUSP**

Puragra Guhathakurta

UCO/Lick Observatory, University of California, Santa Cruz, CA 95064

Electronic mail: raja@lick.ucsc.edu

Brian Yanny

Fermi National Accelerator Laboratory, Batavia, IL 60510

Electronic mail: yanny@sdss.fnal.gov

Donald P. Schneider

Department of Astronomy and Astrophysics

The Pennsylvania State University, University Park, PA 16802

Electronic mail: dps@astro.psu.edu

and

John N. Bahcall

Institute for Advanced Study, Princeton, NJ 08540

Electronic mail: jnb@sns.ias.edu

arXiv:astro-ph/9512015v1 4 Dec 1995

¹ Based on observations with the NASA/ESA *Hubble Space Telescope* obtained at the Space Telescope Science Institute, which is operated by the Association of Universities for Research in Astronomy, Inc., under NASA contract NAS5-26555

ABSTRACT

We describe images of the center of the dense globular cluster M15 (NGC 7078) obtained with the *Hubble Space Telescope* Wide Field and Planetary Camera 2 (WFPC2). Data taken in the F336W, F439W, and F555W filters (approximately U , B , and V) are used to study the surface density distribution of the $\sim 3 \times 10^4$ stars detected in a 5 arcmin^2 region within $r < 2'$ (6.7 pc) of the cluster center. Realistic simulated images have been used to estimate photometric errors and incompleteness in the star counts, which are strong functions of stellar brightness and radius. We have used a combination of point-spread-function fitting and aperture photometry, a technique that yields more accurate photometry than either method alone on the undersampled WFPC2 images of crowded star fields. The error in photometry is $1\sigma \lesssim 0.05 \text{ mag}$ for stars with $V < 18$; this increases to $1\sigma \sim 0.2 \text{ mag}$ at $V = 20.5$, which is 1.5 mag fainter than the main sequence turnoff. The surface density of stars in M15 (after correction for the effects of incompleteness and photometric bias/scatter) is well represented by a power law in radius: $N(r) \sim r^{-0.82 \pm 0.12}$, over the radial range $0''.3$ (0.017 pc) to $6''$. The observed power law is remarkably similar to what is expected if the center of the cluster harbors a massive black hole. Non-parametric estimates of the density profile show a monotonic rise with decreasing radius all the way in to $r = 0''.3$, the smallest radius at which the density can be reliably measured; there is no indication that the profile flattens at smaller radii. Any flat core of radius larger than $2''$ (0.11 pc) in the stellar distribution is ruled out at the $\gtrsim 95\%$ significance level. The star count profile is consistent with that expected from core-collapse models or with the predicted distribution around a massive (few times $10^3 M_\odot$) black hole. The close triplet of bright stars, AC 214, is within $0''.5$ (1.5σ) of the cluster centroid position. The projected density distribution of stars within the central $15''$ of M15 departs from circular symmetry at the 95% level, with an ellipticity $e = 0.05 \pm 0.04$ (90% confidence limits) at a position angle of $+60^\circ \pm 25^\circ$, consistent with the rotation measured by Gebhardt *et al.* (1995) in this region of the cluster.

1. INTRODUCTION

Galactic globular clusters are excellent laboratories for studying the dynamics of dense stellar systems. Theoretical investigations indicate that close binary stars play a critical role in cluster cores, providing energy to prevent or halt core collapse and to drive post-core-collapse expansion (cf. Pryor *et al.* 1989; Heggie & Aarseth 1992; Hut *et al.* 1992a, 1992b). Stellar interactions, including direct collisions and resonant encounters involving binaries, are thought to be common in dense clusters (Benz & Hills 1987; Leonard 1989; Leonard & Fahlman 1991; Hut *et al.* 1992a). Massive black holes would concentrate stars in their vicinity and cause the velocity dispersion to increase (Bahcall & Wolf 1976, 1977). It is difficult, however, to obtain direct observational constraints on the above processes because of the complications caused by the extreme crowding near the centers of high concentration star clusters.

Although there have been a number of investigations of the cores of dense Galactic globular clusters using *Hubble Space Telescope* (*HST*) images [Lauer *et al.* 1991; Paresce *et al.* 1991; Ferraro & Paresce 1993; Guhathakurta *et al.* 1992 (hereafter referred to as Paper I), 1994; DeMarchi & Paresce 1994; Yanny *et al.* 1994a (hereafter Paper II)], most published measurements have been based on data taken with aberrated optics; the size and complex nature of the Point Spread Function (PSF) made it difficult to perform accurate photometry in the inner few arcseconds of the cluster (see above references). The post-repair *HST* data are dramatically improved—the performance of the Wide Field and Planetary Camera 2 (WFPC2) is described by Trauger *et al.* (1994) and we have used this instrument in a recent study of the dense cluster M30 (Yanny *et al.* 1994b, hereafter Paper IV). In this paper, we use WFPC2 images of M15 (NGC 7078) to investigate the stellar density distribution near the center of the cluster. A study of the stellar populations in M15 will be presented later. The photometric error with WFPC2 in the crowded central $1'$ of M15 is a factor of two smaller, and the stellar detection threshold about 2.5 mag fainter, than in comparable exposures with the pre-refurbishment *HST* (Paper II).

About 20% of all globular clusters possess what has been termed ‘post-core-collapse’ morphology, in which the surface brightness appears to rise all the way into the cluster center; M15 belongs to this category (King 1975; Djorgovski & King 1984). Numerical N -body simulations (cf. Heggie 1985) and Fokker–Planck calculations (Grabhorn *et al.* 1992) of core collapse indicate that the resulting projected density profile slope should be between -0.5 and -1.5 . Heating by binary stars can stabilize core collapse (Heggie 1975; Goodman & Hut 1989; McMillan *et al.* 1991) and the core is expected to undergo oscillations even in the absence of binaries (Sugimoto & Bettwieser 1983; McMillan 1989; Murphy *et al.* 1990). These processes are expected to produce a flattening of the stellar density within a region of radius a few percent of the half-mass radius, or 0.05–0.1 pc for a typical globular cluster (Goodman 1989; Gao *et al.* 1991). This range of core radii corresponds to $1''$ – $2''$ at the distance of M15. [We adopt $D = 11.5$ kpc as the distance to M15, based on its horizontal branch apparent magnitude $V_{\text{HB}} = 16.19$ and a line-of-sight reddening of $E_{B-V} = 0.11$ (Fahlman *et al.* 1985).] The high angular resolution of the post-repair *HST* data makes it possible to probe the distribution of stellar surface density on subarcsecond scales and to measure (or place strong constraints on) the size of M15’s core.

In addition, the high central density of M15, one of the highest of known globular clusters (Webbink 1985; Djorgovski 1993), has long made it a candidate for a cluster that has a central black hole (Bahcall *et al.* 1975). A massive compact object in the center of a cluster would produce a surface density ‘cusp’ in the steady-state radial distribution of stars, $\sigma(r)$, with a slope $\alpha \equiv d(\log \sigma)/d(\log r) \sim -0.75$ (Bahcall & Wolf 1976, 1977), in good agreement with the measured slope (as we shall see later). Unless explicitly stated otherwise, we use the term ‘cusp’ in this paper in a phenomenological sense to describe a density profile that is increasing roughly as an inverse power

law of the distance from the center of the cluster. We do not imply by this convenient representation of the data that any particular theoretical solution is preferred.

Lauer *et al.* (1991) used an early, pre-refurbishment *HST* *U* band image of the cluster to study the radial distribution of stars. They found that the diffuse residual light in M15—the component that remains after subtraction of the light of bright, resolved stars—appears to flatten near the cluster center with a core of radius $r_{\text{core}} = 2''.2$. However, analysis of realistic simulated images (Paper II) showed that it is difficult to interpret the significance of the diffuse light in images of M15 obtained with the aberrated *HST*. This uncertainty arises because the software used in the analysis overestimates the brightnesses of stars near the crowded cluster center (as a result of blending) and because of the broad wings of the PSF ($r_{\text{PSF}} \sim 2''.5$). Star counts derived from pre-repair *HST* data were consistent with an $\alpha \sim -0.8$ cusp or with an $r_{\text{core}} \lesssim 2''$ core. Our previous limit on r_{core} (Paper II) did not take into account the covariance between r_{core} and the asymptotic power law index α . Moreover, the systematic effects of a non-uniform stellar detection threshold in the aberrated data made it difficult to assign reliable confidence limits to the density profile. The WFPC2 images of M15 yield a larger and cleaner sample of stars that rule out a core as large as $r_{\text{core}} = 2''$ at the 95% level; the data are well fit by an $\alpha = -0.8$ power law distribution (see Sec. 5).

Even with the $0''.1$ resolution of WFPC2 images, our study of M15’s inner density profile is limited by small number statistics in the star counts because photometric scatter/bias and incompleteness prevent us from probing much below the main sequence turnoff. This fact requires us to use detailed and realistic simulations to investigate various possible systematic errors. While the usual artificial star tests yield an estimate of the fraction of stars detected, a more extensive simulation (such as that described in Sec. 4) is needed to simultaneously correct for both incompleteness and photometric error.

The shape of the stellar density profile near the center of M15 is similar to the predicted distribution around a massive compact object (Bahcall & Wolf 1976). This does not, however, prove that a massive object is present, since the observed profile slope is also within the range of slopes expected for collapsed cores. The definitive way to distinguish between black hole and core-collapse models is to measure the dispersion in stellar radial velocities, σ_v , as a function of radius. In the presence of a black hole, σ_v is expected to increase inwards roughly as $r^{-0.5}$ (Keplerian dependence). If, on the other hand, M15 is undergoing core collapse and does not contain a massive central object, σ_v is expected to be roughly constant over the inner $5''$ at the isothermal value of $\lesssim 15 \text{ km s}^{-1}$ (Heggie 1985). The ground-based velocity data of Peterson *et al.* (1989) are suggestive of a steep rise in σ_v within a few arcminutes of M15’s center, exceeding 20 km s^{-1} in the inner $6''$, consistent with that expected for a central black hole of mass $10^3 M_\odot$ (Bahcall & Ostriker 1975; Bahcall & Wolf 1976, 1977). However, the inward rise in σ_v in the Peterson *et al.* data may not be significant because of the large sampling errors associated with such a measurement (Dubath *et al.* 1994; Dubath & Meylan 1994). With corrective optics (COSTAR) installed on *HST*, it is now possible (though time consuming) to obtain velocities, accurate to a few km s^{-1} , of tens of individual post-main-sequence stars in the central $1''$ of M15. Such data should settle the debate over whether core collapse or a massive black hole causes the stellar concentration at the center of M15.

The observations and relevant characteristics of the data are described in Sec. 2. A new analysis technique, developed specifically for WFPC2 images, is outlined in Sec. 3. In Sec. 4, we describe a simulation that is used to estimate photometric accuracy and degree of completeness in the data. [A reader who is not interested in the details of the procedures used to derive stellar photometry, error estimates, and star count correction factors may wish to skip Sec. 3 and 4.] In Sec. 5, we determine the stellar surface density in M15 as a function of distance from the cluster center using parametric and non-parametric techniques, and test for circular symmetry in the star count distribution. In

Sec. 6, we discuss the implications of the results. A summary is presented in Sec. 7.

2. OBSERVATIONS

A set of 8 WFPC2 images of the center of M15 was obtained on a single orbit on 1994 April 7: 4×8 s with the F555W filter, 2×40 s in F439W, and 2×200 s in F336W. The pointing of the telescope was identical for all 8 exposures. The zero points of the WFPC2 instrumental magnitudes in F336W, F555W, and F785LP have been adjusted so there is rough agreement ($\lesssim 0.1$ mag) with ground-based *UBV* measurements of stars in M15 (Stetson 1994); they are also consistent with the in-orbit WFPC2 calibration (Burrows 1994). We have opted in favor of empirical photometric calibration since the instrumental calibration coefficients change with time, particularly after decontamination events, and are somewhat dependent on the exact set of flat fields used in the processing pipeline. In the rest of this paper, we use the terms *U*, *B*, and *V* interchangeably with the WFPC2 filter designations when referring to the calibrated instrumental magnitudes. The main sequence turnoff, defined to be the bluest point in the main sequence, is at $V_{\text{TO}} = 19.1$. Since our analysis of the density distribution of M15 relies only on measurements of stellar brightness *relative* to V_{TO} , and since stellar mass changes very gradually with *V* magnitude across V_{TO} (Bergbusch & Vandenberg 1992), uncertainties in the photometric zero points or in the definition of the turnoff point are unimportant for this study.

Each WFPC2 image consists of a mosaic of four 800×800 Charge Coupled Device (CCD) frames—a Planetary Camera CCD (PC1) with a scale of $0''.046 \text{ pixel}^{-1}$, and three Wide Field CCDs (WF2–WF4) with scales of $0''.10 \text{ pixel}^{-1}$. The usable field of view is $34'' \times 34''$ for PC1 and about $76'' \times 76''$ for each of the WF CCDs; the total image area is approximately 5.1 arcmin^2 . A greyscale (negative) representation of the full four-CCD mosaic of the combined *V* band image (4×8 s) of M15 is shown in Figure 1. The telescope pointing was chosen so that the cluster center was imaged near the center of PC1 (upper right quadrant). The WF2–WF4 images are oriented counterclockwise starting from upper left. The gaps between the usable fields of view of adjacent CCDs ($\lesssim 1''$ in width) are not shown to scale in Figure 1 and the small inter-CCD rotations ($\lesssim 1^\circ$) are ignored in this representation. A detailed description of the instrumental parameters and in-orbit characteristics of WFPC2 is given by Burrows (1994) and by Trauger *et al.* (1994).

The exposure times are short enough to ensure that the brightest stars in the image ($V \approx 12.5$, $B \approx 13.5$, $U \approx 12.5$) are not saturated by more than a factor of 4–5 in the individual exposures. At most 10 pixels are affected by saturation at the centers of each of these bright stars (more typically 3–4 pixels), and about 10 stars are affected on each CCD frame, but it is possible to recover their magnitudes using information in the PSF wings (Sec. 3).

Figure 2 is a “true color” reproduction of the central $9'' \times 9''$ portion of M15 imaged on PC1. The blue, green, and red intensities are roughly proportional to the logarithm of the flux in the *U*, *B*, and *V* bands, respectively. The cluster center is marked by the green ‘+’ sign (see Sec. 5.1). This section of the image contains 623 post-main-sequence stars with $V < 19$ and over 1600 stars with $V \lesssim 21$ which are detected in all three bands, but star identifications are incomplete for $V > 19$ near the center of the cluster. The average surface density of post-main-sequence stars ($V < 19$) in the central $9'' \times 9''$ region shown in Figure 2 is 7.4 arcsec^{-2} , which corresponds to 2370 pc^{-2} ; the mean surface density within $r < 1''$ is 2.4 times higher than this. The high angular resolution of *HST* images is crucial for the study of such crowded regions, especially for obtaining reliable photometry of stars fainter than the main sequence turnoff.

3. ANALYSIS TECHNIQUE

We have developed and tested procedures for deriving stellar photometry from *HST* images of

dense globular clusters. The reader is referred to Papers I and II for a detailed description. Even though the procedures were originally designed for pre-repair *HST* data with an aberrated PSF, several of the steps are relevant for analysis of crowded star fields and we apply them here.

Standard bias and flat field calibrations have been applied to the data as part of the preprocessing pipeline at the Space Telescope Science Institute. The availability of multiple images in each band, with identical pointings (pointing offsets $< 0''.01$) and exposure times, facilitates removal of cosmic ray events and combination of images, without the need for fractional pixel interpolation. While this observing strategy is essential for the elimination of cosmic rays, it results in a higher effective read noise in the combined image than if the data were obtained as a single long exposure. The detectability and photometry of faint stars, being read noise limited in sparse regions of the image, are thus slightly degraded. The four short *V* band exposures from the first set have been median filtered to remove cosmic rays. In each of the *B* and *U* bands, the difference between the pair of exposures has been used to identify and mask positive excursions in the individual exposures (see Paper IV for details). The individual cosmic ray-cleaned exposures in each band have been averaged excluding masked pixels. All subsequent data analysis makes use of these cosmic ray-free, combined *U*, *B*, and *V* images.

The stellar positions in the *U* and *B* band PC1 images are offset from those in the *V* band PC1 image by 1.1 pixel and 0.5 pixel ($0''.05$ and $0''.02$), respectively. For the WF2–WF4 CCDs, the offset between the *U* and *V* image ranges from 0.3 pixel to 0.5 pixel ($0''.03$ – $0''.05$) and it is about 0.2 pixel ($0''.02$) between *B* and *V*. The combined images in the three bands have been aligned by fractional pixel interpolation and summed to produce a deep image. The undersampling of the PSF, particularly in the WF data, makes interpolation somewhat unreliable; however, the sum of interpolated images is only used for finding stars and not for stellar photometry. For a typical $V \sim 21$ main sequence star, the number of counts (i.e., detected photons) in the *U*, *B*, and *V* images is about the same: the system throughput and intrinsic stellar flux are lower in *U* (and to a lesser extent in *B*) than in *V*, but this is roughly compensated by the longer exposure times at shorter wavelengths. Coadding the *UBV* images lowers the detection threshold for faint main sequence stars by almost 0.6 mag compared to images in a single band.

The standard matched filter peak finding algorithm FIND of the DAOPHOT software package (Stetson 1987) is used to detect stars on the summed $U + B + V$ image. A preliminary round of PSF fitting is done using this star list, a library PSF template, and the ALLSTAR program in DAOPHOT and the residual image (original – template) is inspected. The star list is then manually edited to separate blended stars (typically a few percent of the stars in the list), to add faint stars whose peak brightnesses lie below the FIND detection threshold, and to remove hot pixels and PSF artifacts mistakenly identified as stars. The master list contains 1.2×10^4 stars from the PC1 image (0.33 arcmin^2) and about 9×10^3 , 6×10^3 , and 1.0×10^4 stars from WF2–WF4, respectively (each WF CCD covers an area of 1.56 arcmin^2).

The analysis technique used in this paper incorporates a set of standard DAOPHOT II routines (Stetson 1992). The data analysis (PSF reconstruction, PSF fitting, etc) is done independently for the *U*, *B*, and *V* bands, and independently for each of the four CCD frames in the WFPC2 mosaic. Only the master star list is used as a common starting point for PSF fitting in the three bands.

The data analysis procedure begins by correcting for saturation in the central few pixels of the images of the brightest 5–10 stars in each CCD frame. A small PSF template ($r_{\text{PSF}} = 10$ pixels) is constructed from unsaturated stars, fitted to the unsaturated PSF wings of the saturated stars ($2 \text{ pixels} \lesssim r < 4 \text{ pixels}$), and the results of the fit are used to replace all pixels values above the saturation threshold ($\sim 2.5 \times 10^4$ electrons). A series of iterations is performed on the saturation-corrected images. Each iteration step consists of constructing an empirical PSF template of radius

20 pixels by averaging the images of about 30 relatively isolated, bright stars, after removing the neighbors of these stars using the PSF template from the previous iteration. The quality of the PSF template improves with each iteration as the neighbors of the PSF stars are removed with increasing precision, reaching convergence after 3–4 iterations. Of all the templates tested—bivariate Gaussian, Lorentzian, and Moffat functions with a matrix of fixed or linearly changing residuals—the combination of a Moffat function and residuals which vary linearly with image position produces the best approximation to the actual PSF. The final PSF template is simultaneously fitted to all stars detected on the image using the positions in the master list as input to the ALLSTAR routine in DAOPHOT.

For each star, the results of the ALLSTAR PSF template fit are used to remove every neighboring star within a 40 pixel radius ($2r_{\text{PSF}}$). Aperture photometry of each star is then obtained using a circular aperture of radius 2 pixels for stars on PC1 ($r = 0''.09$) and 1.6 pixels for stars on WF2–WF4 ($r = 0''.16$), with the local sky background measured in a surrounding annulus. These aperture radii represent optimal values as determined from tests conducted on simulated images and on the M15 data, the latter based on the tightness of the red giant branch (RGB) and main sequence in a color–magnitude diagram (CMD). Measurements with smaller apertures lead to noisier photometry due to the effects of undersampling and intra-pixel quantum efficiency variations (Burrows 1994), while photometry from larger apertures are affected to a greater extent by contamination from poorly subtracted neighboring stars. We have experimented with three different photometric techniques on a simulation of the M15 PC1 image (Sec. 4): direct aperture photometry, PSF fitting, and the hybrid of these two methods described above. For bright stars ($V \sim 15$), the hybrid method and aperture photometry yield comparably good results ($1\sigma \sim 0.015$ mag) since the effect of neighbors is negligible (particularly on color measurements), but PSF fitting is significantly less accurate ($1\sigma \sim 0.03$ mag). In fact, PSF fitting is even less accurate for bright stars in the WFPC2 image of M15 ($1\sigma \sim 0.04$ mag, judging from the width of the bright RGB) than for those in the simulated image, because the effect of intra-pixel quantum efficiency variation has not been included in the simulated image and because the PSF is slightly broader, and therefore better sampled in the simulation than in the PC1 image (the broadening is a result of the fact that the simulation PSF template was derived by interpolating between stellar images on the WFPC2 image of M15). Direct aperture photometry of faint stars ($V \sim 19$ – 20) is severely affected by neighbor contamination ($1\sigma \sim 0.45$ mag and the mean photometric bias is 0.25 mag), but the hybrid method and PSF fitting perform better ($1\sigma \sim 0.30$ mag; mean bias = 0.07 mag).

Photometry of a set of bright, isolated stars in a series of concentric apertures indicates that the $r = 2$ pixel aperture contains about 75% of the light contained in an $r = 20$ pixel aperture around the V band PC1 PSF. The enclosed fraction is slightly higher for the $r = 1.6$ pixel WF aperture and for the U and B bands. Differences in the aperture correction are accounted for before combining the PC data with data from the WF CCDs. For a given band and CCD, the fraction of light within the aperture appears to be essentially independent of position on the CCD. The PSF in the M15 PC1 image is somewhat more centrally concentrated than the one in the PC1 image of M30 which was obtained a week earlier than the M15 data (Paper IV). This is probably caused by orbital variations in the *HST* focus, commonly referred to as “breathing” (Trauger *et al.* 1994).

4. SIMULATION

4.1 Construction of the Simulated Image

The high degree of crowding near the center of M15 greatly complicates the stellar photometry and star count analysis. To estimate the errors and biases introduced by crowding, we have constructed a simulated image and have analyzed it in the same manner as the M15 data (cf. Papers I

and II for a description of this procedure). The simulated image is designed to mimic the combined V band M15 PC1 image as closely as possible. We have not simulated the WF data; the stellar density (and degree of crowding) is low enough throughout the WF images to ensure that counts of stars are essentially complete for $V < 20$.

The basic ingredients needed to build the simulated image are: (1) the shape of the stellar luminosity function (LF); (2) the surface density of stars, brighter than some specified limiting magnitude, as a function of projected distance from the cluster center; and (3) the position dependent shape of the stellar PSF. As described below, each of these input parameters is derived from the PC1 V image of M15.

For the purposes of the simulation, the stellar LF is assumed to have the same shape at all radii. The *HST* M15 data show no evidence for luminosity segregation vs. radius. Figure 3 shows the V band LF as a function of radius in M15. The stars detected in the full WFPC2 mosaic are divided into 8 annuli: (1) $r < 5''.4$, (2) $5''.4 \leq r < 9''.8$, (3) $9''.8 \leq r < 15''$, (4) $15'' \leq r < 24''$, (5) $24'' \leq r < 35''$, (6) $35'' \leq r < 48''$, (7) $48'' \leq r < 66''$, and (8) $66'' \leq r < 127''$. The boundaries of these annuli have been chosen so that they contain roughly the same number of $V < 19$ stars; our sample should be nearly complete at all radii for stars brighter than this limiting magnitude (see below). The LF of post-main-sequence stars in M15 has the same shape at all radii, except for the slight deficiency of bright stars in the innermost radial bin. The bump at $V \sim 16$ is caused by horizontal branch (HB) stars. Artificial star tests and previous simulations (Papers II and IV) indicate that the turnover at the faint end of the LF is caused by incompleteness, which is a strong function of distance from the center—the observed LF peaks at $V \sim 19$ (the main sequence turnoff point) in the innermost radial bin, but rises beyond that and peaks about 2 mag fainter in the outermost radial bin. The open circles in Figure 3 show the LF used to construct the simulated image (arbitrary normalization). It is derived from the M15 PC1 data, by averaging the data for bright stars ($V \lesssim 19$), and by adopting the upper envelope of the LFs in the range $V = 19$ –20. For $V > 20$, the LF is assumed to be a power law with a slope $d(\log N)/dV = 0.125$. The details of the shape of the synthetic LF beyond $V = 20$ are unimportant for the purpose of learning about faint stars; the photometric accuracy and detection efficiency for $V > 20$ stars are determined by the local surface density of brighter stars ($V \lesssim 18$) in crowded regions and are limited by read noise and photon noise in sparse portions of the image. Furthermore, the faint end slope of the LF is such that the main sequence luminosity is dominated by stars at the bright end ($V \sim 19$ –20) and the contribution from stars fainter than $V = 20$ is negligible.

The projected density of stars in the simulated image is described by a radial distribution function consisting of two power laws, one with an index $\alpha_1 = -0.7$ within $r < 6''$ of the cluster center and the other with an index $\alpha_2 = -1.3$ for $r > 6''$. This is a good approximation to the shape of the (uncorrected) density profile of bright ($V \lesssim 18$) stars in the inner $30''$ of M15 (see Sec. 5). The PC1 data should be complete for $V < 18$ stars, so their radial distribution is unlikely to be strongly affected by differential incompleteness as a function of distance from the cluster center. The overall normalization of the stellar density in the simulation is the same as in M15: about 6 arcsec^{-2} at $r = 1''$ to a limiting magnitude of $V = 18$.

Each star is assigned a V magnitude based on the synthetic LF, a projected radius based on the dual power law radial distribution function, and a random azimuthal angle. Artificial stellar images are then added to a blank 800×800 frame using a linearly variable PSF template (as defined by Stetson 1987) derived from the M15 PC1 data. The center of the simulated cluster is assumed to be near the center of the frame. Poisson noise and read noise are added to the simulated image based on the instrument characteristics of the PC1 CCD and on the length of the M15 V exposures. The final simulated image is similar (in a statistical sense) to the combined V band image ($4 \times 8 \text{ s}$)

of M15. This image is analyzed using the procedure described in the last section. In the course of the analysis, we deliberately avoid using any input data that were used in the construction of the simulated image. Instead, we use the `FIND` routine to detect stars, reconstruct a PSF template from the detected stars, use `ALLSTAR` to perform PSF-fitting, and derive an aperture magnitude for each detected star after subtraction of its neighbors.

4.2 Photometric Accuracy

The analysis program derives a list of stellar positions and brightnesses from the simulated image; this is referred to as the ‘output list’. Each star in the output list is matched to the star closest to it in the ‘input list’ (the list of positions and magnitudes used to construct the simulated image), provided their positions agree to within 1 pixel ($0''.05$ for PC1; $0''.1$ for the WF images). Essentially all the stars in the output list (over 1.1×10^4 in number) are successfully matched. The difference between the input and output V magnitudes of all matched stars is plotted against the ‘true’ V magnitude (V_{input}) in the top panel of Figure 4. The stars tend to be concentrated near the $V_{\text{output}} = V_{\text{input}}$ line, but their distribution about it is asymmetric. The photometric bias, in the sense of the output magnitudes being systematically brighter than the input ones, is caused by blending in crowded parts of the image: two or more input stars within $\sim 0''.05$ of one another are fit as a single, brighter star. Some of the extreme values of $V_{\text{input}} - V_{\text{output}}$ are mismatches—a small error in astrometry occasionally leads to a configuration where the input star closest to the output star is *not* its true counterpart. The reader is referred to Papers I and II for details.

We divide the sample of matched stars into two parts: stars located within $5''$ of the center of the simulated cluster (13% of all matched stars) and those beyond $5''$. These two subsamples are presented in the middle and bottom panels of Figure 4, respectively. The open circles show the mean magnitude offset in 0.5 mag bins, and the error bars show the 1σ rms dispersion within each bin. The filled circles indicate the median value of $V_{\text{input}} - V_{\text{output}}$, and the error bars include $\pm 34\%$ of the stars on either side of the median (this corresponds to the fraction of points enclosed by 1σ error bars around the peak of a Gaussian distribution). The dashed lines indicate $\pm 10\%$ photometric errors. The large error in the $V = 13.75$ bin in the inner $5''$ (middle panel) is a result of the fact that one of the two stars in this bin is blended with a $V = 14$ star causing its output magnitude to be in error by $+0.6$ mag (upper panel). The asymmetry in the distribution of magnitude differences (photometric bias) is reflected by the fact that the $+34\%$ errors are larger than the -34% errors. It is evident in the top panel of Figure 4 that the distribution peaks close to zero, and the median values are less strongly affected by the positive tail of the distribution than the mean values.

The accuracy with which the analysis program recovers the magnitudes of individual stars in the simulation depends both on the stellar brightness and on the local surface density of stars, the latter being a monotonically decreasing function of distance from the cluster center. In the relatively sparse outer region, $5'' < r < 25''$, the 1σ scatter in photometry is $\lesssim 0.03$ mag for stars with $V < 17$, about 0.1 mag at $V = 18$, and 0.25 mag at $V = 20$, while the mean bias is ≤ 0.1 mag for $V < 20$. By comparison, the 1σ scatter (and mean bias) for stars in the crowded inner $5''$ is about 0.2 mag ($\gtrsim 0.1$ mag) at $V = 18$ and 0.4 mag (0.4 mag) at $V = 20$. The photometric scatter and bias within $r < 5''$ increase rapidly beyond $V = 20$. However, only 30% of the input stars with $V = 20$, and less than 10% of $V = 21$ stars, are detected in this region (see Sec. 4.3). The detected fraction of $V_{\text{input}} > 20$ stars represents the positive tail of the $V_{\text{input}} - V_{\text{output}}$ distribution—those stars for which blending, errors in sky determination, and photon/read noise have caused a large enough brightening (by $\gtrsim 0.5$ mag) for them to be above the detection threshold in the crowded inner region.

Our simulation shows that there are two principal sources of photometric error in the crowded portions of the PC1 image of M15: (1) blending of two or more stars into a single apparent object, and (2) inaccurate subtraction of a close, but resolved, star. The first of these leads to a systematic

bias in photometry while the second can cause positive or negative measurement errors. For $V > 19$ stars within the inner $5''$, the errors caused by blending appear to be comparable to or larger than those caused by improper neighbor removal. The blending biases brightness measurements but not necessarily color measurements, since it mostly affects main sequence stars just below the turnoff, all of which have roughly the same color ($B - V \sim 0.4\text{--}0.5$ for stars in the range $V = 19\text{--}22$).

4.3 Correction of Star Counts

To correct the observed star counts in M15 for incompleteness and photometric error, the input and output star lists from the simulation are compared. We define a star count correction factor:

$$C = \frac{N(V_{\text{output}} < V_{\text{lim}})}{N(V_{\text{input}} < V_{\text{lim}})}, \quad (1)$$

where the input and output stars are counted over the same area. It is important to note that the counts in the numerator and denominator of the above equation are drawn independently from the output and input lists, respectively—they are *not* based on matched star counts. The quantity C measures the full ‘throughput’ of the analysis procedure, including the effects of incompleteness and photometric error, not merely the detection efficiency.

Figure 5 shows C as a function of radial distance r from the cluster center, with the stars binned in $0''.4$ -wide annuli. Three different limiting magnitudes, $V_{\text{lim}} = 18.3, 19.0$, and 20.0 , are used in the top, middle, and bottom panels of Figure 5, respectively. The error bars represent the Poisson error in the number of output stars. While the non-detection of stars decreases the value of C , photometric bias ($V_{\text{output}} < V_{\text{input}}$) tends to increase C , resulting in values greater than unity in some cases. Even in the absence of bias, photometric errors cause more stars to be scattered into a magnitude-limited sample than out of it due to the fact that the stellar LF rises towards fainter magnitudes (Fig. 3). Non-detection of stars dominates over the effect of photometric bias/scatter in the inner few arcseconds for $V_{\text{lim}} \gtrsim 19$. At large radii ($r \gtrsim 10''$) and for $V_{\text{lim}} \lesssim 20$, C approaches unity as 100% of the input stars are detected and the effect of photometric error on the star counts become negligible. In choosing the optimal value of V_{lim} , there is a trade-off between the shot noise associated with the relatively small number of stars at bright limiting magnitudes (which affects both the estimation of C and the M15 star counts), and the strong radial dependence and possible systematic uncertainties in the correction factor at faint limiting magnitudes.

We use an analytic approximation of the form:

$$C(r) = 1 + C_1 e^{-r/r_1} + C_2 e^{-r/r_2} \quad (2)$$

to represent the correction factor derived from the simulation (smooth curves in Fig. 5). The scale length r_1 is set to $5''$ for all values of V_{lim} and the last term is excluded ($C_2 = 0$) for $V_{\text{lim}} = 18.3$. The remaining parameters are: $C_1 = (0.5, 0.8, 0.1)$ for $V_{\text{lim}} = (18.3, 19, 20)$, and $C_2 = (-0.9, -0.85)$ and $r_2 = (1''.5, 2''.5)$ for $V_{\text{lim}} = (19, 20)$. The correction factor for the $18.3 < V < 20.0$ sample is well fit by the parameters $C_2 = -0.95$, $C_1 = 0$, and $r_2 = 2''.5$. In deriving the radial density profile of M15 in Sec. 5, we correct the magnitude-limited star counts by dividing them by the above formulae for $C(r)$.

5. DENSITY DISTRIBUTION

5.1 Cluster Center

The location of the center of M15 is determined by calculating the centroid of the positions of all stars brighter than V_{lim} within a circle of radius r_{lim} . The centroid computation is iterative: the

center of the circle used to define the sample is set to the centroid calculated in the previous iteration. The process converges within 10 iterations for initial guesses within a few arcseconds of the obvious cluster center. Each star is given equal weight in the centroid calculation; unlike estimates based on the surface brightness distribution, a number-weighted centroid is not biased towards the few bright RGB stars that dominate the cluster light (cf. the shape of the bright end of the LF in Fig. 3). The centroid is insensitive to the choice of limiting radius and magnitude for $5'' < r_{\text{lim}} < 15''$ and for $20 < V_{\text{lim}} < 21$. Smaller values of r_{lim} and V_{lim} yield samples containing too few stars to permit accurate determination of the centroid. The mean of the centroids of 10 stellar samples (various combinations of r_{lim} and V_{lim}) is adopted as the cluster center. Its coordinates, relative to the bright reference star AC 211, are:

$$\Delta\alpha_{2000}(\text{center}) = +0''.36 \pm 0''.2; \quad \Delta\delta_{2000}(\text{center}) = -1''.97 \pm 0''.2 \quad (3a)$$

(see Paper II for an explanation of this coordinate system), and the coordinates of AC 211 are given by Kulkarni *et al.* (1990):

$$\alpha_{2000}(\text{AC 211}) = 21^{\text{h}}29^{\text{m}}58^{\text{s}}.26; \quad \delta_{2000}(\text{AC 211}) = +12^{\circ}10'02''.9 \quad . \quad (3b)$$

The rms scatter among the centroids of the 10 samples is $\delta r \sim 0''.3$ (6 pixels on the PC1 image). The error in the centroid of each sample is estimated using the bootstrap resampling method (Efron 1982); it is typically $0''.2$ – $0''.3$. Thus, a conservative measure of the 1σ error in the determination of the cluster center is $0''.3$. If the center we have adopted is off the “true” cluster center by an amount Δr , it will cause a spurious flattening in our estimate of the density profile interior to Δr . We restrict our analysis of the stellar density distribution in M15 to radii larger than the 1σ positional error in the cluster centroid.

There appears to be a local maximum in the projected density of stars about $0''.3$ to the north-west of the cluster center adopted here, within the 1σ error circle for the center. This can be seen as a concentration of faint stars in Figure 2 immediately above the green ‘+’ marking the mean centroid position. Merritt & Tremblay (1994) derived adaptive kernel estimates of the stellar surface density in M15 using pre-refurbishment *HST* data from Paper II, and found a peak at exactly this location, offset to the north-west of the centroid position (see Fig. 12 of their paper). We have *not* adopted the position of the density peak as the cluster center (except for using it as an alternate center) as this would bias our estimate of the radial density profile in the sense of making it as steep as possible near $r = 0$. It is interesting that the object AC 214 (Aurière & Cordoni 1981), which was resolved into a close triplet of horizontal branch stars using early *HST* images (Paper II), is located about $0''.5$ (1.5σ) east of the centroid position.

5.2 Star Counts vs. Radius

Determination of the radial density profile near the center of M15 is the principal motivation for obtaining these high resolution images. Luminous stars serve as a convenient tool for measuring the surface mass density. Ground-based data, such as the *UBVR* images of M15 obtained by Lugger *et al.* (1987) in $1''.5$ seeing, or even Stetson’s (1994) $0''.5$ -seeing images, lack the resolution necessary to study sufficient numbers of individual stars near the dense cluster center. The disadvantage of using the overall surface brightness distribution (Lugger *et al.* 1987) is that it is dominated by a few stars at the tip of the RGB which are not representative of the cluster’s stellar population, not even its post-main-sequence population—*e.g.* most of the light within $r < 1''$ of M15’s center comes from only 7 stars. It is customary to subtract the contribution of the brightest few stars and to analyze the residual diffuse light (cf. Lauer *et al.* 1991). In clusters as dense as M15 though, the residual

light is greatly affected by inaccurate photometry and removal of the bright stars, the errors being largest near the crowded cluster center (see Sec. 3.4 of Paper II for a detailed discussion).

Counts of individual stars are a fairer tracer of the stellar mass density than the luminosity-weighted star distribution, since all post-main-sequence and turnoff stars have roughly the same mass ($M \sim 0.8 M_\odot$) despite the fact that their visual luminosities span over two orders of magnitude. Mass segregation is unimportant for stars brighter than $V \sim 20$ —the Bergbusch & Vandenberg (1992) isochrone for M15 predicts a stellar mass of $M = 0.77\text{--}0.79 M_\odot$ for $V \leq 19$ (above the main sequence turnoff), falling only slightly to $M = 0.74 M_\odot$ at $V = 20$. Magnitude-limited star counts are, however, affected by incompleteness and photometric errors; we correct for these effects with simulations of the data.

We have compared star counts derived from WFPC2 data in the inner region of M15 to those derived from pre-repair HST Planetary Camera data (Paper II). There are 58 stars in the WFPC2 list with $V < 19.0$ (and a total of 82 stars down to $V = 19.6$) within $1''$ of the cluster center, compared to 28 stars with $V < 19.0$ (and a total of 33 stars down to $V = 19.5$) in the pre-repair list for the same region. The two datasets contain 489 stars and 232 stars, respectively, between $1'' < r < 3''$, and 1100 stars and 523 stars, respectively, between $3'' < r < 6''$, down to a limiting magnitude of $V = 20$. The WFPC2 sample of stars in the crowded central region of M15 is more than double the size of the pre-repair sample, and has a more uniform degree of completeness than the latter.

Figure 6 shows the radial distribution of star counts for two independent magnitude-limited samples, $V < 18.3$ and $18.3 < V < 20.0$, within $5''$ of the cluster center in $0''.4$ -wide radial bins. The dashed lines show raw (uncorrected) counts while the open squares show corrected counts, using the analytic approximation to the correction factor $C(r)$ given by Eq. (2). The shapes of the corrected star count profiles for the two samples are consistent with one another to within Poisson errors (error bars in Fig. 6), even though the uncorrected profiles and the $C(r)$ curves derived from the simulated image are quite different for the two. The radial profile shapes of the samples are *expected* to be the same—the average mass of the stars comprising the $V = 18.3\text{--}20$ sample is $M \sim 0.75 M_\odot$ compared to $M = 0.78 M_\odot$ for the $V < 18.3$ sample; this difference in mean stellar mass is too small to expect significant effects due to mass segregation (cf. Bolte 1989; Pryor *et al.* 1986). The similarity in the shapes of the corrected density profiles suggests that the correction factors derived from the simulation are accurate. The counts in the $V_{\text{lim}} = 18.3$ sample are actually corrected *downward*; this is due to the effect of photometric errors on magnitude-limited counts discussed in Sec. 4.3. The $18.3 < V < 20.0$ counts, on the other hand, are increased because incompleteness effects dominate over the error introduced by photometric bias.

For the purpose of making density measurements, we group the stars in M15 into three samples with limiting magnitudes of $V_{\text{lim}} = 18.3, 19.0$, and 20.0 . Magnitude-limited samples are usually dominated by stars with $V \approx V_{\text{lim}}$ since the typical stellar LF rises steeply towards the faint end (Fig. 3). For example, at $r = 5''$, the $V < 18.3$ sample constitutes less than 45% of the $V < 19.0$ sample and only 16% of the $V < 20.0$ sample. Interior to $0''.4$, however, the high degree of crowding causes most stars fainter than $V = 18.3$ to go undetected, implying that the three samples are nearly identical in this region. The star count correction factor C within $r < 0''.4$, on the other hand, is quite different for these samples (see Fig. 5). Even though the raw counts in the three samples are *not* independent of one another, the corrected star count profiles derived from them provide complementary measures of the density of M15. The use of a bright limiting magnitude ($V_{\text{lim}} = 18.3$) has the advantage that $C(r)$ is not a strong function of radius—it changes by less than 30% within $r < 5''$. The disadvantage is that Poisson errors in the star counts are relatively large. The reverse is true for the $V_{\text{lim}} = 20.0$ sample: it is limited not by Poisson statistics but by

uncertainties in the count correction factor coupled with the fact that C departs strongly from unity near the cluster center. The $V_{\text{lim}} = 19.0$ sample represents a reasonable compromise between these two sources of uncertainty.

Figure 7 shows the corrected $V_{\text{lim}} = 19.0$ and 20.0 stellar density profiles (open squares and ‘ \times ’, respectively) with 1σ Poisson error bars based on the raw counts. The $V < 20.0$ counts have been shifted down by 0.6 dex to match the normalization of the $V < 19.0$ sample. The data in the range $0''.3 < r < 5''$ are consistent with a power law density profile, $\sigma(r) \sim r^\alpha$, with the index $\alpha = -0.82$ (curve 1). A core of radius $r_{\text{core}} = 1''$ (0.06 pc) or smaller is allowed by the data but a $2''$ core appears to be ruled out. Note that curves 2 and 3 in Figure 7 are of the form:

$$\sigma(r) = \sigma_0 [1 + C_\alpha (r/r_{\text{core}})^2]^{\alpha/2} \quad , \quad (4a)$$

where

$$C_\alpha = 2^{-2/\alpha} - 1 \quad . \quad (4b)$$

This form of $\sigma(r)$ approaches a power law with index α for $r \gg r_{\text{core}}$, while the core radius r_{core} has the usual property that the surface density at this radius is half the central density σ_0 . The asymptotic index α is set to -0.8 for curves 2 and 3, the value that best fits M15 data in the range $r = 2''\text{--}5''$.

When comparing the M15 star count profile to model curves, it should be noted that the estimate of the stellar density within $r < 0''.3$ (to the left of the dotted vertical line in Fig. 7) is likely to be biased low due to errors in the determination of the cluster center. To test how sensitive the estimate of the density profile is to the choice of cluster center, we have adopted the location of the stellar concentration $0''.3$ to the north-west of the cluster centroid (Fig. 2; Sec. 5.1) as an alternate cluster center. The bold dashed line in Figure 7 shows the corrected density profile of $V < 19.0$ stars in M15 about this alternate center; it is consistent with the profile measured relative to the centroid (open squares) to within Poisson errors.

Stars from the entire WFPC2 mosaic image of M15 are used to determine the stellar surface density distribution from the center out to $r = 2'$. This radial density profile is plotted in Figure 8. Only $V < 19$ stars are shown, with no correction for incompleteness/photometric error. These corrections are small for $V_{\text{lim}} = 19$ and for $r \gtrsim 5''$. The uncorrected profile is well fit by a combination of three power law sections: an inner index $\alpha_1 = -0.7$ within $r < 6''$; $\alpha_2 = -1.3$ in the range $6'' < r < 30''$; and $\alpha_3 = -2$ for $r > 30''$. The stellar surface density profile beyond $r = 30''$ in M15 follows the r^{-2} slope (dotted line) expected for $r \gg r_{\text{core}}$ in an isothermal profile. The solid lines in Figure 8 indicate the radial distribution function used to construct the simulated image (Sec. 4.1). The apparent dip in the profile at $r = 13''$ may be a result of inaccurate photometry of stars imaged near the gap between PC1 and the WF CCDs.

5.3 Parametric Fits to the Radial Density Distribution

In this section, we compare the radial distribution of stars in the inner $5''$ of M15 to various model profiles. The model profiles have been multiplied by the correction function $C(r)$ [Eq. (2)] in order that they may be fitted directly to the raw (uncorrected) magnitude-limited counts. Unlike direct estimates of the stellar density for which the data must be divided by $C(r)$ (a procedure that can be uncertain if C is much less than unity), this approach attaches low weight to the model in regions where C is small. Another attractive feature of parametric model fitting is that the stars do not need to be binned into annuli.

Figure 9 shows the cumulative radial distribution $f_{\text{cum}}(r)$ of $V < 19$ stars in M15 (thin stepped line):

$$f_{\text{cum}}(r) = \frac{N(r_{\text{min}} < r' < r)}{N(r_{\text{min}} < r' < r_{\text{max}})} \quad . \quad (5)$$

The minimum radius r_{\min} is set to $0''.3$, the 1σ positional error in the cluster centroid, in order to restrict the sample to stars for which the radial distance is reasonably well determined. We adopt an outer boundary of $r_{\max} = 5''$ since we are interested in the shape of the density profile near the center of the cluster. The smooth bold curve in the upper panel shows the best fit power law while the bold dashed curves represent profiles which have only a 1% Kolmogorov–Smirnov probability of being consistent with the data: $\alpha = -0.82 \pm 0.12$. The bold dashed curves in the lower panel of Figure 9 are profiles with $r_{\text{core}} = 1''$ (upper curve) and $r_{\text{core}} = 2''$ (lower curve), with the asymptotic index α for both models set to -0.82 [Eq. (4)]. Neither of these models is as good a fit to the data as the $\alpha = -0.82$ profile with $r_{\text{core}} = 0$ (bold solid line in upper panel). This does not, however, imply that the presence of a $1''$ core is ruled out. There is finite covariance between r_{core} and α ; this implies that the two parameters must be fitted simultaneously to the data in order to derive a meaningful estimate of the allowed range of parameter space.

Using the functional form given in Eq. (4), we carry out a two parameter (r_{core}, α) maximum likelihood fit to the M15 star count distribution. We fit the $V < 19.0$ and $V < 20.0$ samples separately, multiplying the model by the corresponding star count correction factor $C(r)$ in each case [Eq. (2)]. Standard χ^2 tables for two parameter functional fits are used to derive error estimates for r_{core} and α . The results of the maximum likelihood analysis are shown in Figure 10 in the form of 50%, 75%, 90%, 95%, and 99% confidence contours. These confidence levels do not take into account uncertainties in the determination of the correction factor. There is a significant degree of covariance between the core radius r_{core} and the asymptotic power law index α for both samples. The $V < 20.0$ data are consistent with a pure power law profile ($r_{\text{core}} = 0$), with a best fit index of:

$$\alpha = -0.82 \pm 0.12 \quad (95\% \text{ confidence limits}) \quad . \quad (6a)$$

A profile with a flat core of radius:

$$r_{\text{core}} < 2'' \text{ (0.11 pc)} \quad (95\% \text{ upper limit}) \quad (6b)$$

can also be accommodated by the data but only by making the asymptotic index α steeper—i.e., more negative—than ~ -1 . The 90% upper limit on r_{core} is $1''.8$ (0.10 pc). The $r_{\text{core}} = 2''.2$ profile, which appeared to be a good fit to the diffuse U -band residual light in the deconvolved pre-repair HST image (Lauer *et al.* 1991), is ruled out at the 99% level by WFPC2 star counts.

The allowed region of $r_{\text{core}}-\alpha$ space is roughly similar for the $V_{\text{lim}} = 19.0$ and $V_{\text{lim}} = 20.0$ samples. The $V_{\text{lim}} = 20.0$ sample contains about 2.5 times as many stars (raw counts) as the $V_{\text{lim}} = 19.0$ sample between $2'' < r < 5''$, so that the index α is better constrained. The limits on r_{core} derived from the two samples are comparable: the $V < 20.0$ sample contains only 40% more stars (raw counts) than the $V < 19.0$ sample within $r < 2''$, and its $C(r)$ curve drops sharply with decreasing radius in this region (see Fig. 5), implying that the innermost $2''$ gets low relative weight in the maximum likelihood fit. Errors in estimating $C(r)$ have a bigger effect on the $V < 20.0$ sample than on the $V < 19.0$ sample since the correction factor is closer to unity for the latter sample.

5.4 Non-parametric Estimates of the Radial Density Profile

In the last two sections, the shape of the density profile was estimated by binning the stars in M15 in $0''.4$ -wide radial bins and by fitting model profiles to the radial distribution of stars. Merritt & Tremblay (1994) argue in favor of non-parametric methods for estimating the density profile over the above techniques since the stars need not be grouped (binning introduces an arbitrary degree of smoothing into the data) and it is not necessary to compare the data to specific, parameterized model density profiles. These authors describe the non-parametric MAXimum PENalized Likelihood

(MAPEL) scheme which merely requires that the profile be smooth ‘locally’ (in the radial domain). The degree of smoothness is specified by the λ parameter; the larger the value of λ , the more closely does the estimate approach a ‘smooth solution’. The penalty function, which defines what is meant by a ‘smooth solution’, is a power law in radius. Thus, in the limit $\lambda \rightarrow \infty$, one obtains a single power law, maximum likelihood fit to the star counts. Ideally, λ should be large enough so that the solution is smooth, but not so large as to bias the solution. The number of data points in the sample may be used to determine the optimal value of λ (Thompson & Tapia 1990; Merritt & Tremblay 1994).

We have applied the MAPEL method to the stellar distribution in the inner $5''$ of M15. In Figure 11, we present non-parametric estimates of the surface density profile derived from the $V_{\text{lim}} = 18.3, 19.0$, and 20.0 samples. The dashed lines are based on uncorrected counts while the solid lines are based on applying the correction factor $C(r)$ measured from the simulation (Sec. 4.3). Stars within $0''.3$ of the cluster centroid, for which the radial distance and correction factor are uncertain, are excluded from the analysis. Note the striking similarity in the shapes of the corrected profiles, despite the differences between the uncorrected ones. Smoothing parameters of $\lambda = 1 \times 10^{-4}$, 5×10^{-5} , and 2×10^{-5} are close to optimal for the $V < 18.3$, $V < 19.0$, and $V < 20.0$ samples, respectively (Merritt, private communication).

The non-parametric estimates of the surface density profile in M15 can be used to check the validity of the parametric fits. In general, probabilities derived from Kolmogorov–Smirnov tests and maximum likelihood fits should be treated with a degree of caution. A low probability merely implies that the model is a poor fit to the data, without specifying what aspect of the model is different from the data. Parametric fits can yield spuriously low probabilities if the functional *form* of the model is not a good approximation to the data. A comparison between the shapes of curves 2 and 3 in Figure 7 and that of the corrected MAPEL estimates of M15’s density profile (Fig. 11) shows that the functional form given in Eq. (4) does represent the data well.

Merritt & Tremblay (1994) derive confidence intervals for the surface density by generating a large sample of “bootstrap” samples from the MAPEL estimate (cf. Scott 1992; Taylor 1989). We have applied this method to stars with $V < 19.0$ within $5''$ of the center of M15. Figure 12 shows the non-parametric projected density profile corrected for the effects of incompleteness and photometric error (bold solid line), along with 90% (bold dashed line) and 98% (bold dotted line) confidence bands. The open circles show the density profile relative to the alternate center, $0''.3$ to the north-west of the centroid (at the location of the concentration of faint stars); this profile is indistinguishable from the profile centered on the centroid of the stellar distribution. An upper limit to the core radius may be estimated by considering the lowest allowable central density, $\log[\sigma(0)] \sim 1.2$. The largest radius at which the density is consistent with being half the central value, or at which $\log(\sigma) \sim 0.9$, is about $2''$. This is consistent with the 95% upper limit on r_{core} derived from maximum likelihood fitting (Sec. 5.3).

We have used Merritt & Tremblay’s MAPEL method to derive a non-parametric estimate of the corrected *spatial* density of stars $\rho(r)$ as a function of physical radius (in pc). This is shown in Figure 13 (bold solid curve) for $V < 19$ stars within 0.6 pc ($r < 10''$) of the center of M15. As before, data within 0.017 pc ($r < 0''.3$) are excluded from the analysis, and a smoothing parameter $\lambda = 5 \times 10^{-5}$ is used. The bold dashed and dotted lines indicate 90% and 98% confidence limits; these limits are slightly less stringent than those on the projected density profile (Fig. 12). It is remarkable that the spatial density of M15 at a radius of 0.02 pc approaches 10^5 stars pc^{-3} in post-main-sequence stars alone. Note, the spatial density profile is more relevant than the projected one in constraining models.

5.5 Ellipticity of the Isodensity Contours

The standard picture of globular clusters being non-rotating systems is beginning to change—recent kinematical studies have demonstrated that several clusters exhibit a small, but significant amount of rotation in their inner parts. Gebhardt *et al.* (1995) have used an imaging Fabry-Perot spectrophotometer to map the velocity profile of the integrated light in M15 as a function of position and determine a rotation amplitude of $v_c = 2 \text{ km s}^{-1}$ within $r < 10''$ of the cluster center. The position angle of the major axis of the velocity field (perpendicular to the axis of rotation) is roughly $+40^\circ \pm 20^\circ$ relative to north. They find that the velocity field derived from individual stellar velocities inside $r < 30''$ has a comparable rotation amplitude and orientation. In M15’s central $5''$, Gebhardt *et al.*’s Fabry-Perot integrated light measurements and Peterson *et al.* (1989) long-slit spectrum indicate a rotation amplitude as high as 5 km s^{-1} . Of these, the integrated light data within $r < 10''$ are the least affected by sampling errors. The line-of-sight stellar velocity dispersion is $\sigma_v \sim 12 \text{ km s}^{-1}$ in the inner $r < 10''$ region of M15 (Dubath & Meylan 1994; Gebhardt *et al.* 1994), and this implies a ratio of $v_c/\sigma_v = 0.17$.

For an isotropic oblate rotator, the virial theorem predicts that the isodensity contours should have an ellipticity $e \sim (v_c/\sigma_v)^2$ (Binney 1978), which corresponds to $e \sim 3\%$ for the $r < 10''$ region of M15. Gebhardt *et al.* (1995) have applied an adaptive kernel smoothing technique to stars detected in pre-refurbishment *HST* images of M15 (Paper II) in order to map the isopleths of the stellar density (see also Merritt & Tremblay 1994). The authors remark that the isopleths in the $r < 10''$ region appear to have too high an ellipticity compared to the value of 3% expected from the observed rotation. However, the extended nature of the PSF in the aberrated images ($r_{\text{PSF}} \sim 2''.5$) implies that any estimate of the local stellar surface density derived from these images is difficult to interpret. A bright star tends to produce a “hole” in the distribution since faint stars ($V \sim 19$) are undetectable in its vicinity, yet faint stars dominate the sample in regions away from bright stars. The isopleths measured by Gebhardt *et al.* may be distorted by a handful of bright RGB stars (this is analogous, but opposite in sign, to the effect these stars have on the overall light distribution). The PSF in WFPC2 images has practically no extended structure—thus, these images yield a more uniform sample down to a fainter stellar detection threshold than aberrated *HST* images.

We have used the WFPC2 $V < 20.0$ sample of stars to determine the ellipticity e of the surface density distribution within $r \lesssim 15''$ of the center of M15. An elliptical model distribution, with a radial density profile of the form given by Eq. (4), is fit to the data as described in Sec. 5.3, except that the radial distance r is replaced by the elliptical radial distance parameter:

$$\tilde{r} = [(x/q)^2 + (yq)^2]^{1/2} \quad , \quad (7a)$$

where

$$q = (1 - e)^{1/2} \quad . \quad (7b)$$

The (x, y) axes define the minor and major axes of the model, respectively. A grid of ellipticities e and position angles are fit to the data, while r_{core} and α are held fixed at the optimal values derived from the azimuthally symmetric fit. Beyond $r = 5''.8$, the radial density profile is assumed to be a power law with index $\alpha_2 = -1.3$ (Fig. 8). The models are multiplied by the analytical approximation to the star count correction factor $C(r)$ given in Eq. (2) before fitting to the observed (uncorrected) stellar distribution.

Figure 14 shows the best fit e and position angle (\times) along with 75%, 90%, and 99% confidence contours for these parameters based on a maximum likelihood fit to M15 stars in the radial ranges: $0''.5 < r < 5''.8$ (upper left panel), $5''.8 \leq r < 10''$ (upper right), and $10'' < r < 15''$ (lower left). The combined $0''.5 < r < 15''$ sample (lower right panel) contains nearly 5000 stars and has an

ellipticity $e = 0.05 \pm 0.04$ (90% confidence limits) at a position angle of $+60^\circ \pm 25^\circ$ (measured north through east). This is consistent with the ellipticity and orientation expected on the basis of the observed rotation in the $r < 10''$ region of the cluster, to within the errors of both sets of measurements. The hypothesis of azimuthal symmetry in the $r < 15''$ distribution is rejected at the 95% significance level. It is reassuring that each of the three independent radial subsamples yields maximum likelihood values of e and position angle that agree with the values determined from the combined sample. The Poisson noise in an individual subsample is too large to permit independent determination of e as a function of radius.

6. DISCUSSION: THE CENTRAL CUSP

The $0''.1$ resolution of WFPC2 images makes it possible to study the crowded inner few arcseconds of M15 at a level of detail that is beyond what has been achieved with even the highest resolution ground-based images (cf. Stetson 1994) or with pre-repair *HST* images (Lauer *et al.* 1991; Paper II). As many as 58 stars with $V < 19$ and 82 stars with $V < 20$ are detected in the WFPC2 dataset within the central $r < 1''$ circle alone. This allows determination of the stellar surface density profile on subarcsecond scales near the cluster center.

As discussed in the preceding subsections, the radial projected density profile of M15 rises as a power law towards the center, all the way in to $r = 0''.3$. Given the finite number of stars in any globular cluster, no matter how dense, there is a minimum radius within which the lack of resolved stars and/or extreme crowding limit the ability to determine: (1) the cluster center, (2) the observed (uncorrected) central density, and (3) the star count correction factor. For our WFPC2 data of M15, this minimum radius is about $0''.3$. The density profile of M15 shows no signs of levelling off in the radial range over which it can be reliably measured (see Figs. 6 and 11). Poisson errors in the star counts, however, make it impossible to rule out the presence of a small core: profiles with $r_{\text{core}} < 1''.8$ are consistent with the data at the $\gtrsim 10\%$ level (Sec. 5.3). The data do not *require* a finite r_{core} ; non-parametric estimates of the density profile are best approximated by profiles with $r_{\text{core}} < 1''$. These limits on r_{core} are likely to be biased high due to errors in the determination of the cluster centroid. The half-light (and presumably half-mass) radius r_h of M15 is $61''$ (Djorgovski 1993), so a core radius of $1''$ (0.06 pc) corresponds to $0.016 r_h$. Energy injection by close binary stars or the bounce of a core-collapsed cluster is expected to produce a core whose radius is a few percent of r_h (Goodman 1989). Grabhorn *et al.*'s (1992) Fokker-Planck simulation of M15 suggests that the core radius is larger than $1''$ 95% of the time and larger than $1''.5$ about 75% of the time. This is roughly consistent with the limits on r_{core} imposed by the observations.

The shape of M15's star count profile, r^α with $\alpha = -0.82 \pm 0.12$, is remarkably similar to the $\alpha = -0.75$ steady-state solution calculated by Bahcall & Wolf (1976, 1977) for the radial distribution of equal mass stars around a point mass. The radial extent over which a point mass affects the orbits of stars (roughly twice the "gravitational radius" r_g defined in Paper I) is proportional to its mass. The density profile in M15 is well approximated by an $\alpha = -0.8$ power law out to $r = 6''$, beyond which it steepens to $\alpha_2 = -1.3$ (Fig. 8), a value significantly different from the Bahcall & Wolf solution for a compact object. If we assume that the power law cusp in M15 is the result of a central black hole, the mass of the black hole M_{BH} must be about $10^4 M_\odot$ in order to affect the stellar distribution out to $r \sim 6''$ (see Fig. 10 of Paper II). In fact, this represents an upper limit to the black hole mass since larger values of M_{BH} would cause the profile slope at $r > 6''$ to be shallower than the measured value.

A more restrictive upper limit on M_{BH} comes from measurements of the line-of-sight velocity dispersion σ_v near the center of M15. Peterson *et al.* (1989) found $\sigma_v \sim 25 \text{ km s}^{-1}$ in the inner few arcseconds of the cluster; this constrains M_{BH} to be less than about $3 \times 10^3 M_\odot$. The integrated

stellar absorption line profile near the center of M15, however, is likely to be dominated by a few bright stars and this makes the determination of σ_v uncertain (Zaggia *et al.* 1992, 1993; Dubath *et al.* 1994). Recent long-slit spectroscopy of the central $5'' \times 8''$ region of M15 by Dubath & Meylan (1994) suggests that the velocity dispersion at a radius of $3''$ is about $12 \pm 3 \text{ km s}^{-1}$. This is consistent with the 90% upper limit of $\sigma_v < 16 \text{ km s}^{-1}$ at the same radius derived by Gebhardt *et al.* (1994) with their Fabry-Perot data. If the *central* value of σ_v is as low as these recent studies indicate, the upper limit on the central black hole mass is $M_{\text{BH}} \lesssim 10^3 M_\odot$. Such a black hole would only affect the stellar distribution out to $r \sim 1''$. The underlying distribution (i.e., that which would exist in the absence of a black hole) must then be a power law in the range $1'' \lesssim r \lesssim 6''$ in order to match the observations. The fact that M15's density profile is smooth through the $r = 1''$ region, extending all the way out to $r = 6''$ without significant departures from an $\alpha = -0.8$ power law, makes the case for a $M_{\text{BH}} < 10^3 M_\odot$ central black hole less compelling.

The measured slope of the surface density profile in M15 is also well within the range of slopes expected during and after the process of core collapse: $-0.5 \lesssim \alpha \lesssim -1.5$ (Grabhorn *et al.* 1992; Heggie 1985). An important discriminant between clusters with a central compact mass and those without is the central velocity dispersion of the stars. Since the nature of core collapse is such that it is a “cooling” process, it does not result in a prominent increase in σ_v towards smaller radii. By contrast, a central massive black hole causes the dispersion to increase in Keplerian fashion with decreasing radius, $\sigma_v \propto r^{-0.5}$ (Bahcall & Wolf 1976). The high angular resolution provided by post-repair *HST* optics should facilitate the measurement of M15's central velocity dispersion and thereby resolve the ambiguity.

The ground-based kinematic measurements of Gebhardt *et al.* (1994) and Dubath *et al.* (1994) were obtained in about $1''$ seeing. Even if M15 contains a cusp of stars with a high velocity dispersion but with a radial extent smaller than about $0''.5$, the light of nearby bright RGB stars would dominate the absorption line profile causing the cusp to be masked in the ground-based datasets. There is an unusual object, AC 214, located within $r = 0''.5$ (1.5σ error circle) of the cluster centroid, that was resolved into at least three stars in pre-refurbishment *HST* images (Paper II). WFPC2 data confirm that the three stars each have a brightness of $V \sim 15.5$ and are separated by only $0''.1$ (10^3 AU in projection). If the velocity differences between members of this triplet are found to be high ($\Delta v > 40 \text{ km s}^{-1}$), it would provide strong evidence for a $\gtrsim 10^3 M_\odot$ compact mass in their midst. There is also a small clump of fainter stars with a size of $\sim 0''.2$ located $0''.3$ to the north-west of the cluster centroid (Fig. 2); it is possible that this stellar agglomeration marks the exact location of M15's density cusp.

Independent evidence in favor of a mass concentration near the center of M15 comes from accurate timing measurements of two millisecond pulsars. While most millisecond pulsars have a positive intrinsic period derivative \dot{P} (“spin down”), the fact that these two have a negative \dot{P} suggests that the pulsars are being accelerated towards the cluster center at a high rate. The observed period derivative provides a lower limit on the mass surface density within the central $1''.1$ of M15 of $\sim 4 \times 10^5 M_\odot \text{ pc}^{-2}$ (Phinney 1993), which corresponds to $M > 4.5 \times 10^3 M_\odot$ within this region.

There are 82 stars with $V < 20$ detected within $r < 1''$ of the center of M15 in the WFPC2 images, and our simulation predicts an incompleteness correction factor $1/C = 2.5$ (see Fig. 5). A typical post-main-sequence or turnoff star ($V \lesssim 20$) has a mass of $0.75 M_\odot$ (Bergbusch & Vandenberg 1992). The $V < 20$ stars account for about $150 M_\odot$. The amount of mass in stars fainter than $V = 20$ is not well constrained by the data. The diffuse light of such stars is much fainter than the light of the giants; the process of subtracting the RGB light and measuring the residual light is very uncertain. If the stellar mass function in the center of M15 rises as steeply towards lower masses as it does in the outer parts of the cluster, main sequence stars would be expected to contribute more than ten

times as much mass as is found in $V < 20$ stars. For example, the Bergbusch & Vandenberg 15 Gyr metal poor isochrone for a Salpeter mass function [$N(m) \propto m^{-(1+x)}$, with $x = 1.35$], normalized to contain $150 M_\odot$ in stars brighter than $V = 20$ ($M_V < 4.8$), predicts nearly $4 \times 10^3 M_\odot$ down to a lower mass limit of $0.2 M_\odot$. Their model LF is a very good approximation to the shape of the LF of post-main-sequence stars ($V < 19$) beyond $r > 1'$ in M15 (where the data are complete down to $V = 21$; see Fig. 3), but overpredicts the number of $V = 21$ stars by $\sim 50\%$. More importantly, mass segregation is expected to cause the mass function to be shallower in the center than it is in the outskirts. Phinney (1993) argues that most of the $4.5 \times 10^3 M_\odot$ needed to produce the pulsar acceleration cannot be in the form of very low mass stars and must be primarily in the form of dark remnants (white dwarfs and neutron stars). Concentrating most of the mass in one compact central object of mass $\gtrsim 10^3 M_\odot$ would also explain the pulsar acceleration data.

7. SUMMARY

1. We have obtained F336W, F439W, and F555W (approximately UBV) photometry of more than 3×10^4 stars in the central 5 arcmin^2 ($r < 2'$) of the dense globular cluster M15 (NGC 7078), using *Hubble Space Telescope* Wide Field and Planetary Camera 2 images. A new analysis technique has been applied to the data—one that combines point spread function fitting and aperture photometry. This paper describes measurement of the surface density distribution of the cluster based on V magnitude-limited samples of stars.
2. A realistic simulated image has been constructed. This image has been analysed in the same manner as the M15 WFPC2 data. Photometric accuracy in the inner $15''$ of M15 is estimated to be $1\sigma \lesssim 0.1 \text{ mag}$ for stars with $V < 20$, which is 1 mag below the main sequence turnoff. The simulation is used to quantify the effect of incompleteness and photometric error on magnitude-limited star counts so that the M15 samples may be corrected. Star identifications are nearly complete for $V < 19$ even in the dense cluster center.
3. The number-weighted centroid of the stellar distribution, calculated from samples of various limiting magnitudes and radii, is used to define the center of M15. The 1σ positional error in the cluster center is about $0''.3$. The triple star AC 214 lies about $0''.5$ (1.5σ) east of the cluster centroid, while a dense concentration of faint stars is located $0''.3$ north-west of the centroid.
4. We have presented three complementary approaches to measuring the surface density distribution in M15: binned star counts, parametric fits, and non-parametric estimates. The projected density profile of post-main-sequence stars, corrected for incompleteness and photometric error, is well approximated by a power law, r^α , with $\alpha = -0.82 \pm 0.12$ (95% limits) in the range $0''.3 < r < 6''$. The density appears to rise smoothly towards the center over this region of the cluster with no suggestion of levelling off. More than 80 stars are detected within the central $r = 1''$ circle in M15; this permits reliable determination of the density profile in the range $0''.3 < r < 1''$. Uncertainties in the cluster centroid position and in the star count correction factor, along with Poisson error in the counts, restrict the analysis of M15's surface density profile to $r > 0''.3$. The 95% upper limit on the core radius is $2''$.
5. The profile slope in the inner $6''$ of M15 is very similar to that expected for the stellar distribution around a black hole with a mass of a few times $10^3 M_\odot$. The observed density profile is also consistent with core-collapse models. High angular resolution kinematical measurements are required to distinguish between these two possibilities.
6. The stellar distribution within $r \lesssim 15''$ of the center of M15 shows a 5% ellipticity, and departs from circular symmetry at the 95% level. The shape and orientation of the isodensity contours

are consistent with the amplitude and direction of rotation observed by Gebhardt *et al.* (1995) in the inner parts of this cluster.

We would like to thank D. Merritt for providing MAPEL routines, P. Stetson for providing DAOPHOT II software, and M. Dickinson for assistance in the preparation of the color image. We acknowledge useful discussions with M. Bolte, K. Gebhardt, P. Hut, T. Lauer, D. Merritt, and H.-W. Rix. P.G. would like to thank the Institute for Advanced Study for its generous hospitality. This work was supported in part by NASA through grant number NAG5-1618 and by STScI grant GO-5324.01-93A.

REFERENCES

- Aurière, M., & Cordoni, J.-P. 1981, *A&AS*, 46, 347
- Bahcall, J. N., Bahcall, N. A., & Weistrop, D. 1975, *Astrophys. Lett.*, 16, 159
- Bahcall, J. N., & Ostriker, J. P. 1975, *Nature*, 256, 23
- Bahcall, J. N., & Wolf, R. A. 1976, *ApJ*, 209, 214
- Bahcall, J. N., & Wolf, R. A. 1977, *ApJ*, 216, 883
- Benz, W., & Hills, J. G. 1987, *ApJ*, 323, 614
- Bergbusch, P. A., & Vandenberg, D. A. 1992, *ApJS*, 81, 163
- Binney, J. J. 1978, *MNRAS*, 183, 501
- Bolte, M. 1989, *ApJ*, 341, 168
- Burrows, C. J. (Ed.) 1994, *Wide Field and Planetary Camera 2 Instrument Handbook*, Version 2.0, Space Telescope Science Institute publication
- DeMarchi, G., & Paresce, F. 1994, *ApJ*, 422, 597
- Djorgovski, S. G. 1993, in *Structure and Dynamics of Globular Clusters*, edited by S. G. Djorgovski and G. Meylan (ASP Conf. Series, No. 50), p. 373
- Djorgovski, S. G., & King, I. R. 1984, *ApJ*, 277, L49
- Dubath, P., Meylan, G., & Mayor, M. 1994, *ApJ*, 426, 192
- Dubath, P., & Meylan, G. 1994, *A&A*, 290, 104
- Efron, B. 1982, *The Jackknife, the Bootstrap, and Other Resampling Plans* (Philadelphia: SIAM)
- Fahlman, G. G., Richer, H. B., & Vandenberg D. A. 1985, *ApJS*, 58, 225
- Ferraro, F. R., & Paresce, F. 1993, *AJ*, 106, 154
- Gao, B., Goodman, J., Cohn, H. N., & Murphy, B. W. 1991, *ApJ*, 370, 567
- Gebhardt, K., Pryor, C., Williams, T. B., & Hesser, J. E. 1995, *AJ*, 110, 1699
- Gebhardt, K., Pryor, C., Williams, T. B., & Hesser, J. E. 1994, *AJ*, 107, 2067
- Goodman, J. 1989, in *Dynamics of Dense Stellar Systems*, edited by D. Merritt (Cambridge University Press, New York), p. 183
- Goodman, J., & Hut, P. 1989, *Nature*, 339, 40
- Grabhorn, R. P., Cohn, H. N., Lugger, P. M., & Murphy, B. W. 1992, *ApJ*, 392, 86
- Guhathakurta, P., Yanny, B., Bahcall, J. N., & Schneider, D. P. 1994, *AJ*, 108, 1786
- Guhathakurta, P., Yanny, B., Schneider, D. P., & Bahcall, J. N. 1992, *AJ*, 104, 1790 (Paper I)
- Heggie, D. C. 1975, *MNRAS*, 173, 729
- Heggie, D. C. 1985, in *Dynamics of Star Clusters*, Proc. IAU Symposium No. 113, edited by J. Goodman and P. Hut (Reidel, Dordrecht), p. 139
- Heggie, D. C., & Aarseth, S. J. 1992, *MNRAS*, 257, 513
- Hut, P., *et al.* 1992a, *PASP*, 104, 681
- Hut, P., McMillan, S., & Romani, R. W. 1992b, *ApJ*, 389, 527

- King, I. R. 1975, in Dynamics of Stellar Systems, Proc. IAU Symposium No. 69, edited by A. Hayli (Reidel, Dordrecht), p. 99
- Kulkarni, S. R., Goss, W. M., Wolszczan, A., & Middleditch, J. M. 1990, ApJ, 363, L5
- Lauer, T. R., *et al.* 1991, ApJ, 369, L45
- Leonard, P. J. 1989, AJ, 98, 217
- Leonard, P. J., & Fahlman, G. G. 1991, AJ, 102, 994
- Lugger, P. M., Cohn, H. N., Grindlay, J. E., Bailyn, C. D., & Hertz, P. 1987, ApJ, 320, 482
- McMillan, S. L. W. 1989, in Dynamics of Dense Stellar Systems, edited by D. Merritt (Cambridge University Press, New York), p. 207
- McMillan, S. L. W., Hut, P., & Makino, J. 1991, ApJ, 372, 111
- Merritt, D., & Tremblay, B. 1994, AJ, 108, 514
- Murphy, B. W., Cohn, H. N., & Hut, P. 1990, MNRAS, 245, 335
- Paresce, F., *et al.* 1991, Nature, 352, 297
- Peterson, R. C., Seitzer, P., & Cudworth, K. M. 1989, ApJ, 347, 251
- Phinney, E. S. 1993, in Structure and Dynamics of Globular Clusters, edited by S. G. Djorgovski and G. Meylan (ASP Conf. Series, No. 50), p. 141
- Pryor, C., Smith, G. H., & McClure, R. D. 1986, AJ, 92, 1358
- Pryor, C., McClure, R. D., Hesser, J. E., & Fletcher, J. M. 1989, in Dynamics of Dense Stellar Systems, edited by D. Merritt (Cambridge University Press, New York), p. 175
- Scott, D. W. 1992, Multivariate Density Estimation (New York: Wiley)
- Stetson, P. B. 1987, PASP, 99, 191
- Stetson, P. B. 1992, in Astronomical Data Analysis Software, edited by D. M. Worrall, C. Biemesderfer, and J. Barnes (ASP Conf. Series, No. 25), p. 297
- Stetson, P. B. 1994, PASP, 106, 250
- Sugimoto, D., & Bettwieser, E. 1983, MNRAS, 204, 19P
- Taylor, C. C. 1989, Biometrika, 76, 705
- Thompson, J. R., & Tapia, R. A. 1990, Nonparametric Function Estimation, Modeling, and Simulation (Philadelphia: SIAM)
- Trauger, J. T., *et al.* 1994, ApJ, 435, L3
- Webbink, R. F. 1985, in Dynamics of Star Clusters, Proc. IAU Symposium No. 113, edited by J. Goodman and P. Hut (Reidel, Dordrecht), p. 541
- Yanny, B., Guhathakurta, P., Bahcall, J. N., & Schneider, D. P. 1994a, AJ, 107, 1745 (Paper II)
- Yanny, B., Guhathakurta, P., Schneider, D. P., & Bahcall, J. N. 1994b, ApJ, 435, L39 (Paper IV)
- Zaggia, S., Capaccioli, M., & Piotto, G. 1993, A&A, 278, 415
- Zaggia, S., Capaccioli, M., Piotto, G., & Stiavelli, M. 1992, A&A, 258, 302

FIGURE CAPTIONS

FIG. 1. Greyscale representation of the median of four V band *HST* WFPC2 images (each with an exposure time of 8 s) of the central region of M15. The WFPC2 mosaic covers an area of 5 arcmin^2 and consists of a $34'' \times 34''$ PC1 CCD image and three WF CCD images each $80''$ on a side. The gaps shown in the figure do not accurately represent the slight rotations and actual gaps between the fields of view of adjacent CCDs. The cluster center is located in the PC1 CCD. The scale and orientation of the image are indicated in the upper right.

FIG. 2. A “true color” (24-bit) image of the central $9'' \times 9''$ region of M15 imaged on the PC1 CCD. The red, green, and blue intensities are proportional to the brightnesses in the V , B , and U bands, respectively. Bright red giant branch stars with $B - V \sim 1.3$ appear reddish orange while blue horizontal branch stars with $B - V \sim 0$ appear blue. A green cross marks the cluster center determined from the number-weighted centroid of stellar positions. This image has the same orientation as Figure 1. The surface density of stars is clearly seen to increase towards the cluster center all the way in to radii less than $0''.5$. The X-ray source AC 211 is the very blue star located roughly $2''$ north of the cluster center. There is a concentration of faint stars $0''.3$ north-west of the cluster centroid. The triple star AC 214 is the white object $0''.5$ east of the center; its three components appear blended together in this picture.

FIG. 3. Luminosity function of stars in bins of increasing radial distance from the center of M15. The turnover at faint magnitudes is due to incompleteness. The limits of the radial bins have been chosen so that they include equal numbers of stars brighter than $V = 19$, the main sequence turnoff point. The extrapolated luminosity function used for the simulations in Sec. 3 is plotted as open circles (arbitrary normalization). The bump at $V \sim 16$ is caused by horizontal branch stars.

FIG. 4. Photometric error as a function of V magnitude as determined from our simulation of the M15 PC1 image. The top panel shows the difference between the input (“true”) and output (measured) magnitude for each of $\gtrsim 10^4$ artificial stars. The distribution is skewed towards positive values at faint magnitudes—i.e., the measured magnitudes are systematically too bright—as a result of blending. Stars are divided into two broad radial bins, $r < 5''$ (middle panel) and $5'' < r < 20''$ (bottom panel), and are grouped into 0.5 mag bins in order to compute the mean photometric bias and 1σ rms scatter (open circles and error bars). The median bias is indicated by solid dots and the associated error bars mark the range that includes $\pm 34\%$ of the stars on either side of this median value. (A slight horizontal shift has been introduced between the open and solid symbols for the sake of clarity.) The dashed horizontal lines indicate error levels of ± 0.10 mag. The 1σ photometric error beyond $r > 5''$ is about 0.03 mag down to $V = 17$ and about 0.2 mag at $V = 20.5$, and the magnitude bias is negligible for $V < 21$. In the inner regions, the photometric error and bias are significantly worse than in the outer regions for $V > 17$, and degrade rapidly beyond $V = 20$.

FIG. 5. Star count correction factors [Eq. (1)] derived from the simulation for stars with $V < 18.3$ (top), $V < 19.0$ (middle), and $V < 20.0$ (bottom). The points are based on ratios of binned star counts, the error bars indicate Poisson errors in the number of output stars, and the smooth curves are the exponential approximations given by Eq. (2). At bright limiting magnitudes, $C(r)$ exceeds unity due to the effects of photometric scatter/bias and a steeply rising LF (Sec. 4.3), while incompleteness dominates at faint magnitudes.

FIG. 6. The surface density of stars in the inner $5''$ of M15 binned into $0''.4$ -wide annuli, for two independent samples: $V < 18.3$ and $18.3 < V < 20.0$. The dashed lines are based on uncorrected (raw) counts while the bold open squares have been corrected for the effects of incompleteness and photometric error. Poisson errors (1σ) in the raw counts are indicated. The shapes of the corrected density profiles derived from the two samples are similar, even though their raw count profiles are very different.

FIG. 7. Corrected density of star counts versus radius in the central $5''$ of M15 for $V < 19.0$ (bold open squares) and $V < 20.0$ (crosses). The latter have been divided by a factor of 4 (0.6 dex) to match the $V < 19.0$ profile. (For the sake of clarity, the two sets of data points have also been shifted by a small amount along the horizontal axis relative to each other.) For comparison, we plot a power law profile with $\alpha = -0.82$ (curve 1), and profiles with $r_{\text{core}} = 1''$ (curve 2) and $2''$ (curve 3) using the formula in Eq. (4) with the asymptotic slope set to -0.8 . The $r_{\text{core}} = 2''$ profile appears to be inconsistent with the M15 data. It is important to note that estimates of the density interior to $r < 0''.3$ (dotted vertical line) are likely to be biased low due to uncertainties in the position of the cluster center. The bold dashed line shows the corrected $V < 19.0$ density profile measured relative to an alternate cluster center, one that is located $0''.3$ north-west of the centroid.

FIG. 8. Stellar surface density profile of M15 covering the full radial range ($r < 100''$) available on the WFPC2 image. All $V < 19$ stars are plotted with no correction for the effects of incompleteness/photometric error. The uncorrected data are well fit by three power law segments, with indices of $\alpha = -0.7$, -1.3 , and -2.0 (steepening with increasing radius) and transition radii of $r_{\text{break}} = 5''.8$ and $30''$. The solid lines trace the distribution function used in the construction of the simulated image.

FIG. 9. Cumulative radial distribution of $V < 19$ stars between $0''.3 < r < 5''$ from the center of M15 (thin stepped line). Data interior to $r = 0''.3$ are excluded since our estimate of the density there is likely to be biased by errors in the centroid determination. The upper panel shows power law model profiles with $\alpha = -0.70$, -0.82 , and -0.95 , while the lower panel shows profiles with cores of radii $r_{\text{core}} = 1''$ and $2''$ and an asymptotic power law index $\alpha = -0.8$ [Eq. (4)]. All model profiles have been multiplied by the exponential approximation to the star count correction factor [Eq. (2)].

FIG. 10. Results of maximum likelihood fitting of a two-parameter (r_{core}, α) family of model profiles, of the form given by Eq. (4), to stars between $0''.3 < r < 5''$ in M15. The upper and lower panels present $V_{\text{lim}} = 19.0$ and 20.0 samples, respectively. Alternate dashed and solid lines mark 50%, 75%, 90%, 95%, and 99% confidence contours. There is significant covariance between the core radius and asymptotic slope. An $\alpha = -0.82 \pm 0.12$ (95% limits) power law fits the data well. An $r_{\text{core}} = 2''$ profile is ruled out at the 95% level.

FIG. 11. Non-parametric estimates of the stellar surface density in M15 obtained by applying Merrit & Tremblay's (1994) MAXimum PENalized Likelihood (MAPEL) method. Three stellar samples with $V_{\text{lim}} = 18.3$, 19.0 , and 20.0 are presented. Dashed lines represent uncorrected profiles, while solid lines have been corrected by dividing by $C(r)$ from Eq. (2). The three corrected profiles are remarkably similar in shape. The profiles show no indication of levelling off at small radii. Their shapes are well approximated by the analytical form given in Eq. (4).

FIG. 12. Non-parametric MAPEL estimate of the surface density of $V < 19.0$ stars in M15 (solid line), corrected for incompleteness/photometric error, with 90% (bold dashed line) and 98% (bold

dotted line) confidence bands. The open circles show the density profile measured relative to an alternate cluster center, located $0''.3$ north-west of the centroid. An $r_{\text{core}} = 2''$ profile can barely be accommodated within the confidence bands. The most likely value of the core radius, however, is $< 1''$.

FIG. 13. The *spatial* density of post-main-sequence stars in M15 (solid line), a non-parametric (MAPEL) estimate based on the corrected $V < 19.0$ sample, plotted against the radial distance in parsec. The bold dashed and dotted lines indicate 90% and 98% confidence limits, respectively. The data are unreliable interior to $r = 0.02$ pc ($0''.3$). The central density of post-main-sequence stars in M15 appears to exceed 10^5 stars pc^{-3} .

FIG. 14. Results of maximum likelihood fitting to determine the ellipticity e and position angle of the stellar isodensity contours in M15. Stars are grouped into three radial bins: $0''.5 < r < 5''.8$ (upper left panel), $5''.8 < r < 10''$ (upper right), and $10'' < r < 15''$ (lower left). The full sample ($0''.5 < r < 15''$) is shown in the lower right panel. The ‘x’ marks the best fit values of the parameters, while the contours indicate 75%, 90%, and 99% confidence boundaries. The number of stars in the set is indicated. The combined sample has an ellipticity $e = 0.05$ at a position angle of $+60^\circ$ east of north. The probability of the stellar distribution in this sample being azimuthally symmetric is only 5%. While the radial subsamples contain too few stars to permit accurate determination of e and the position angle, the maximum likelihood solution for each is consistent with that of the combined sample.

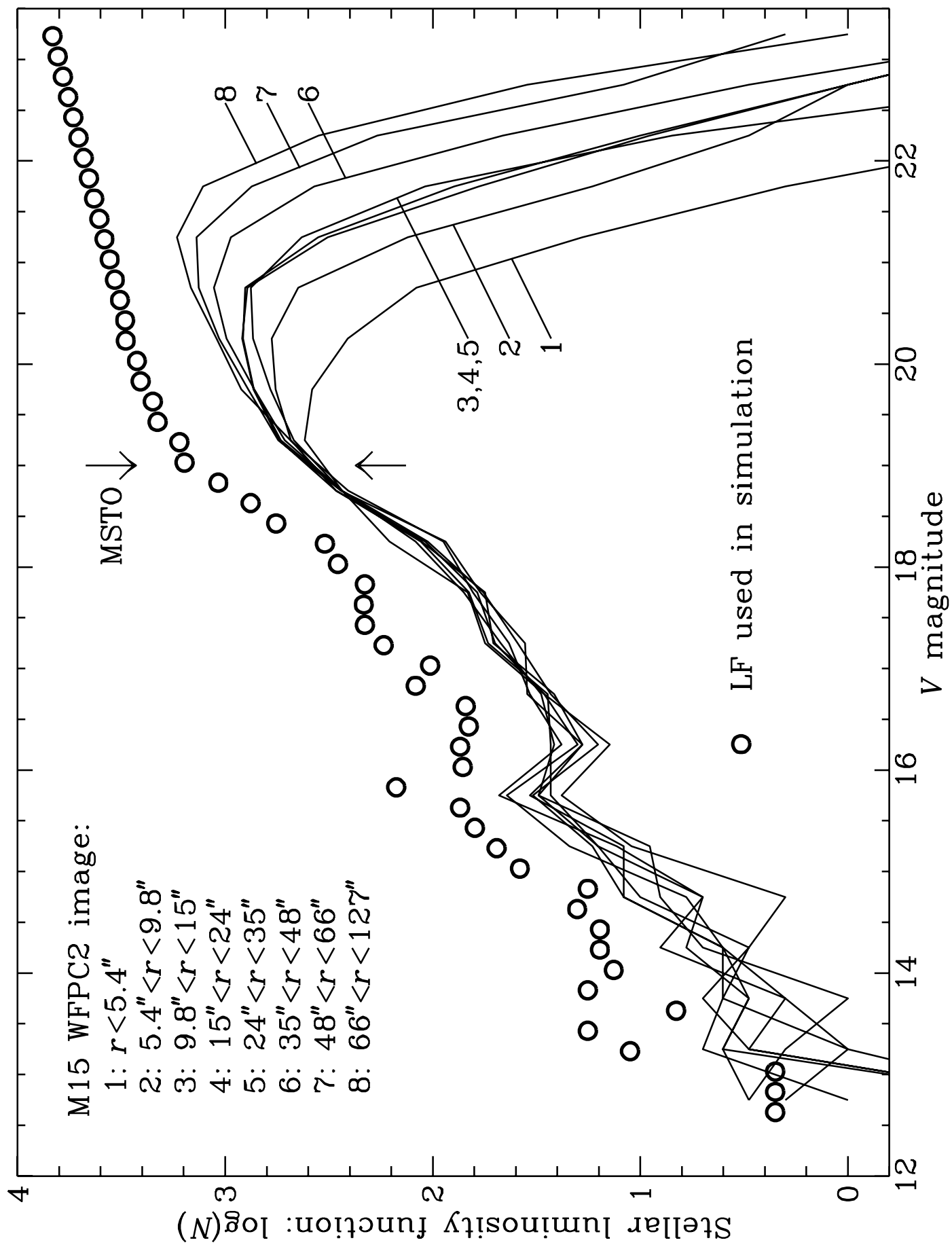


Fig. 3

Simulation of M15 PC1 image

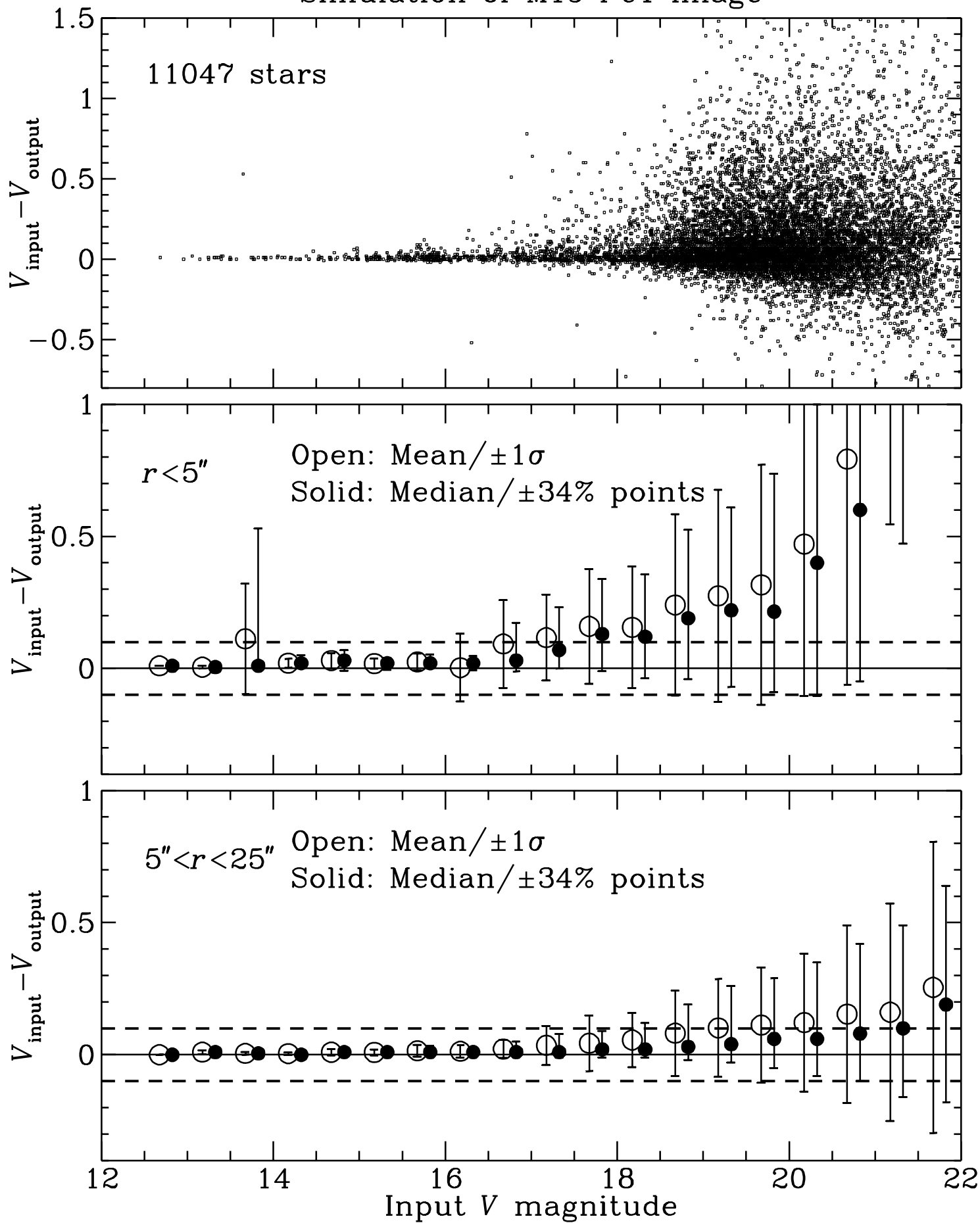


Fig. 4

Simulation of M15 PC1 image

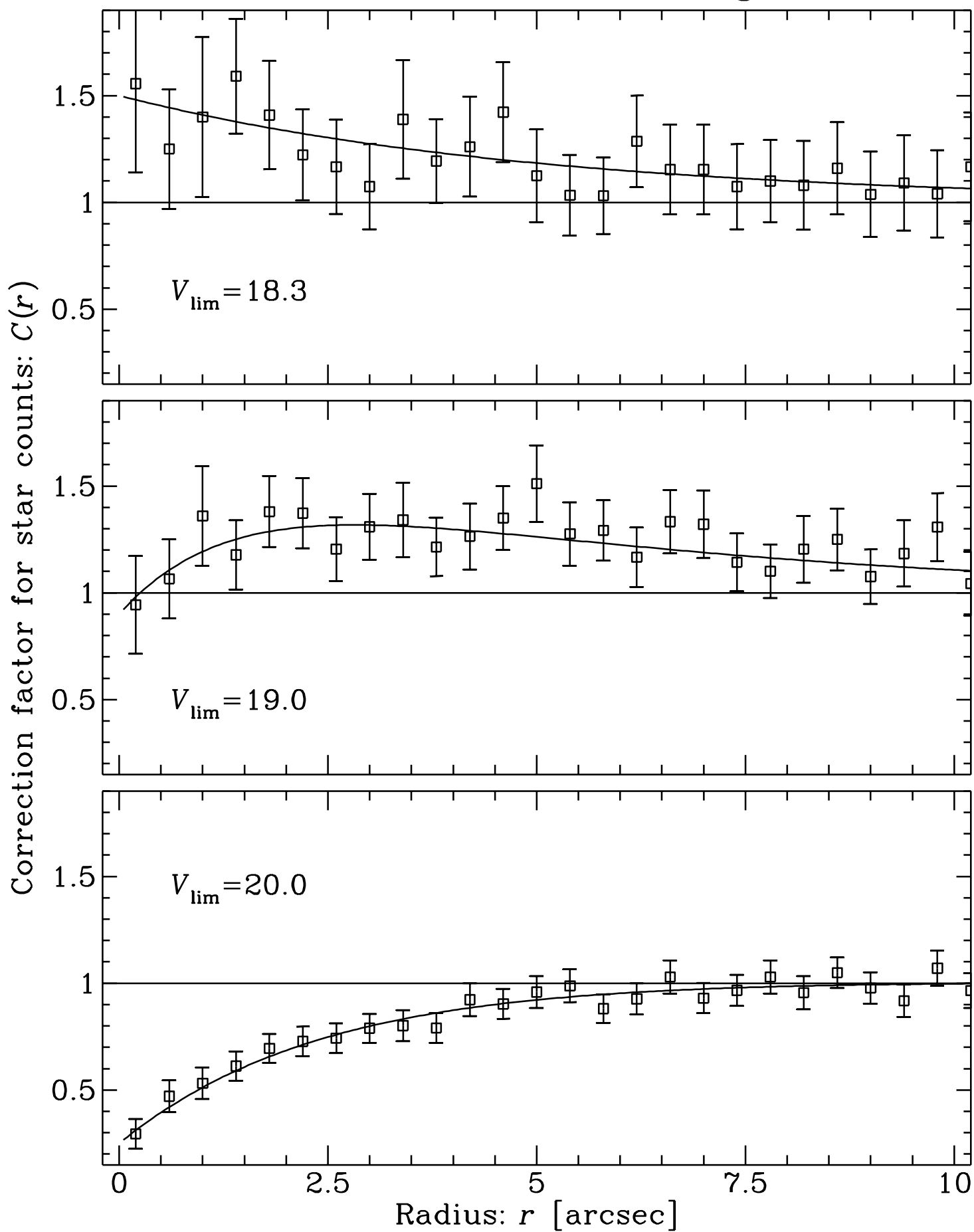


Fig. 5

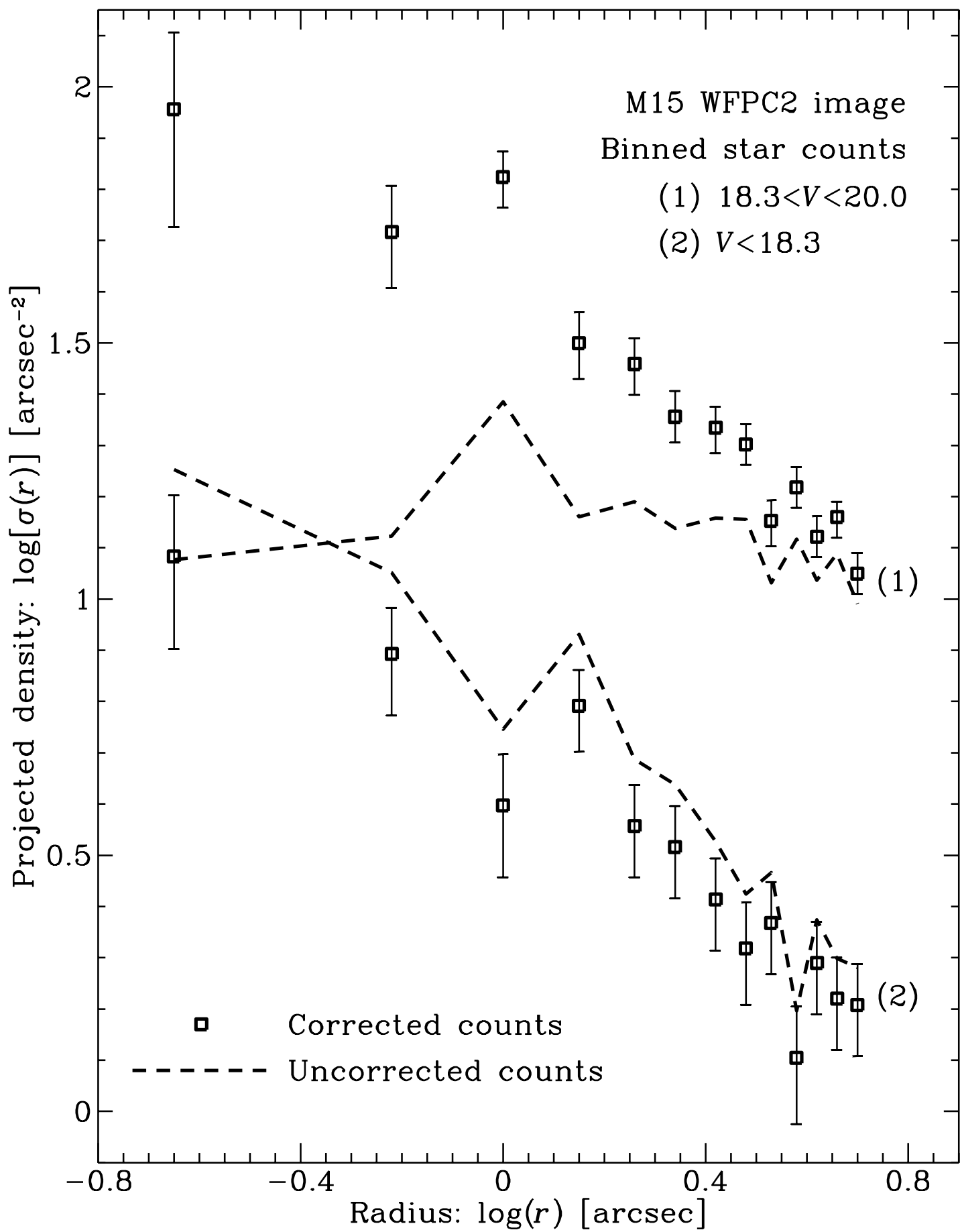


Fig. 6

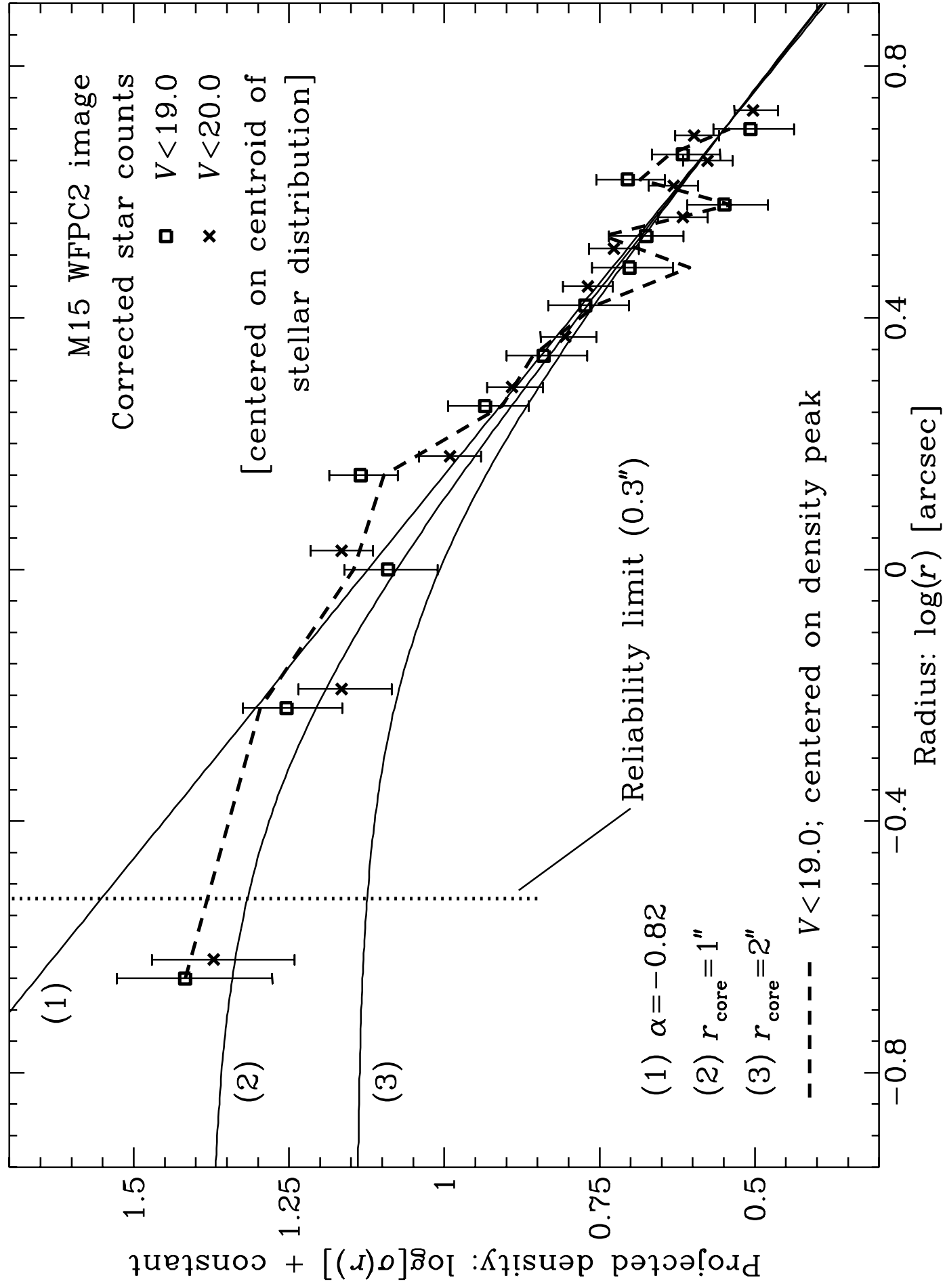


Fig. 7

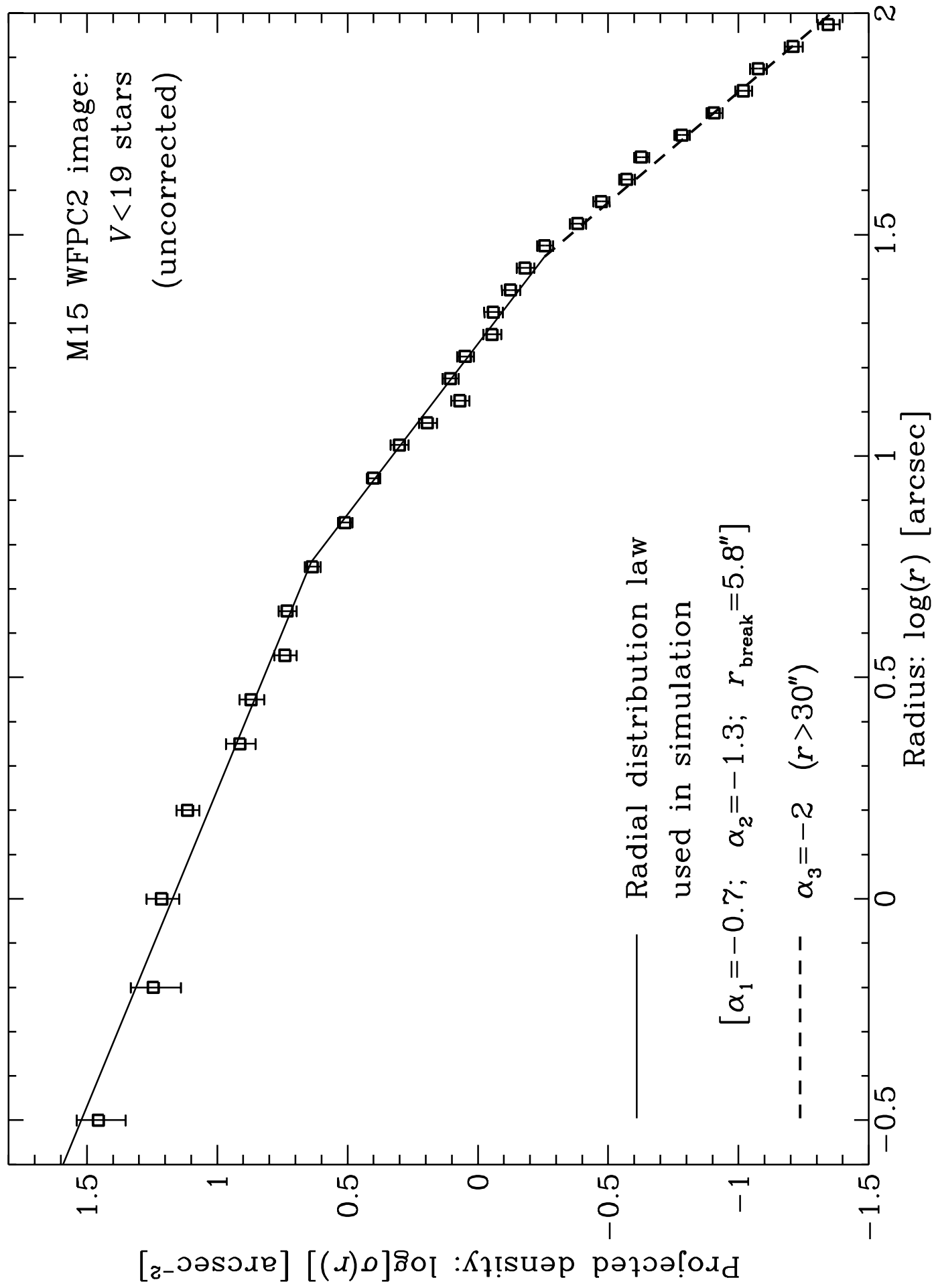


Fig. 8

M15 WFPC2 image

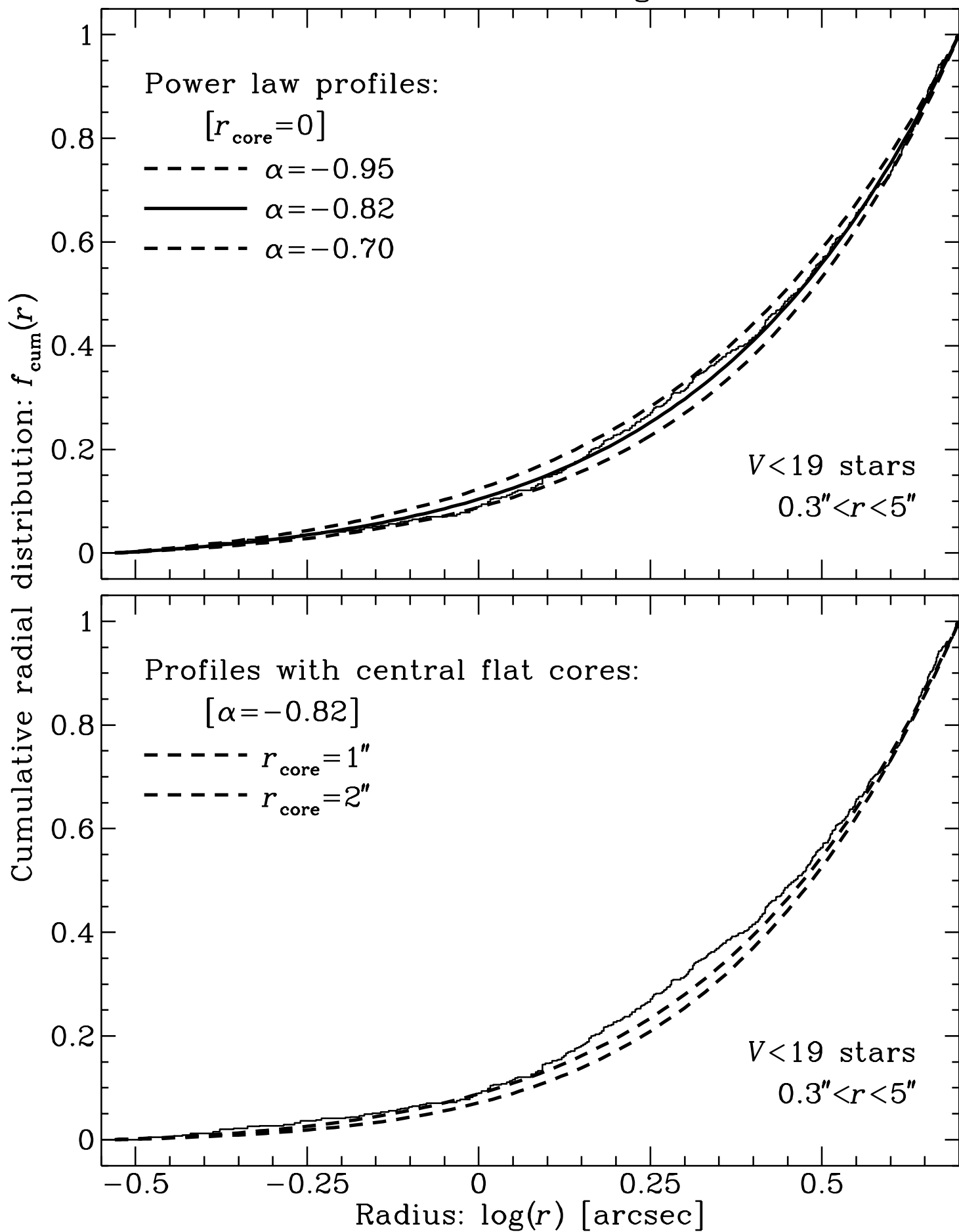


Fig. 9

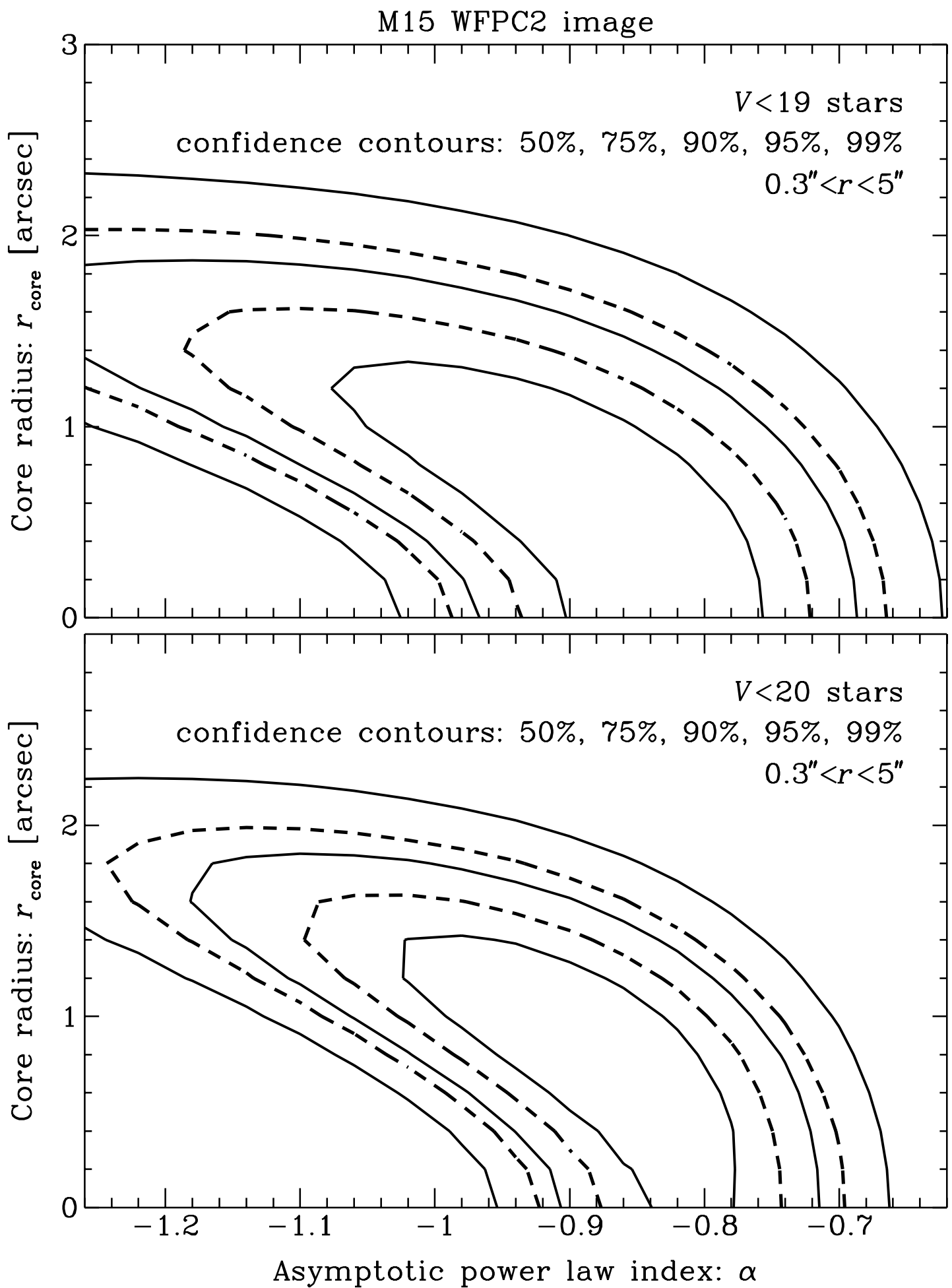


Fig. 10

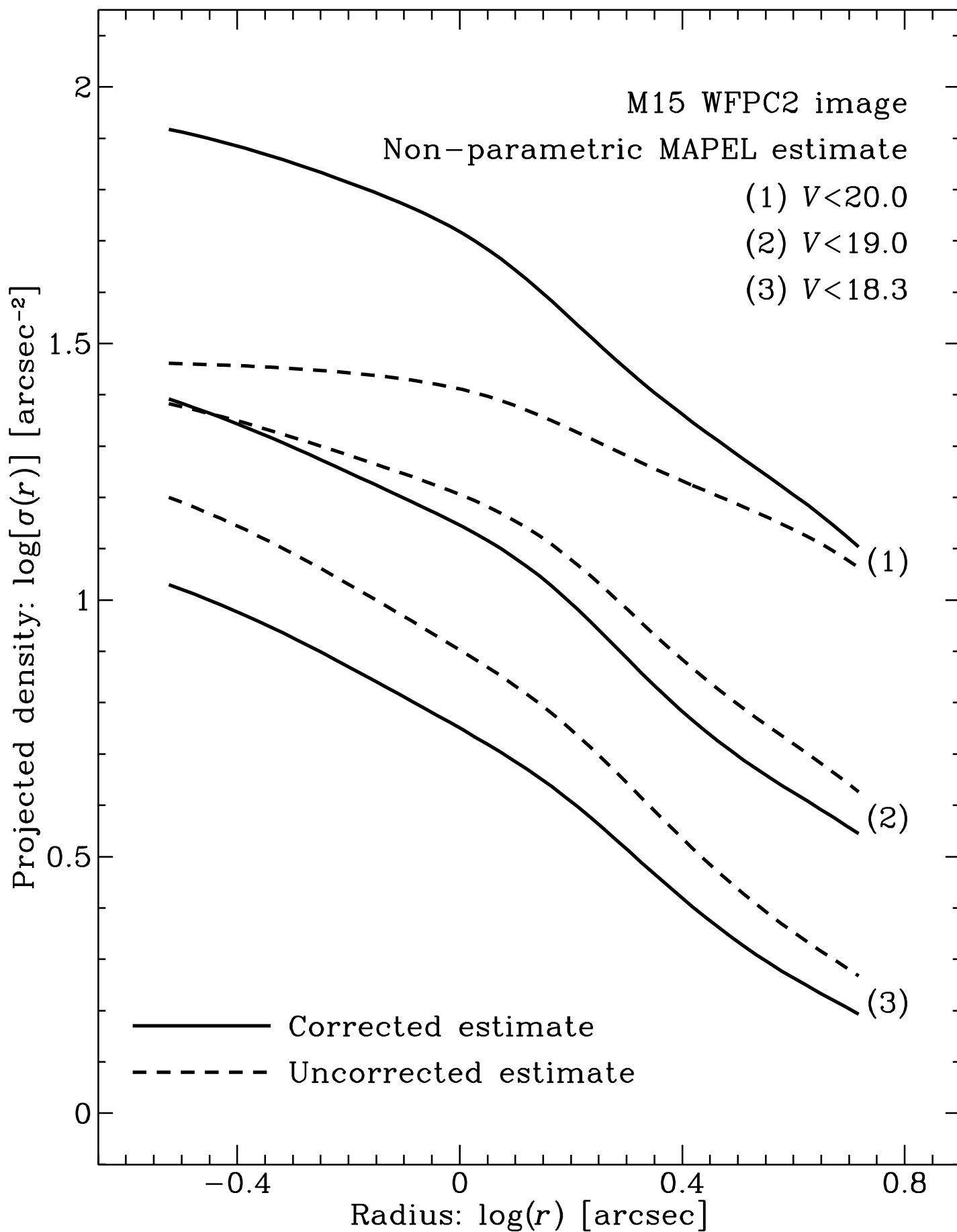


Fig. 11

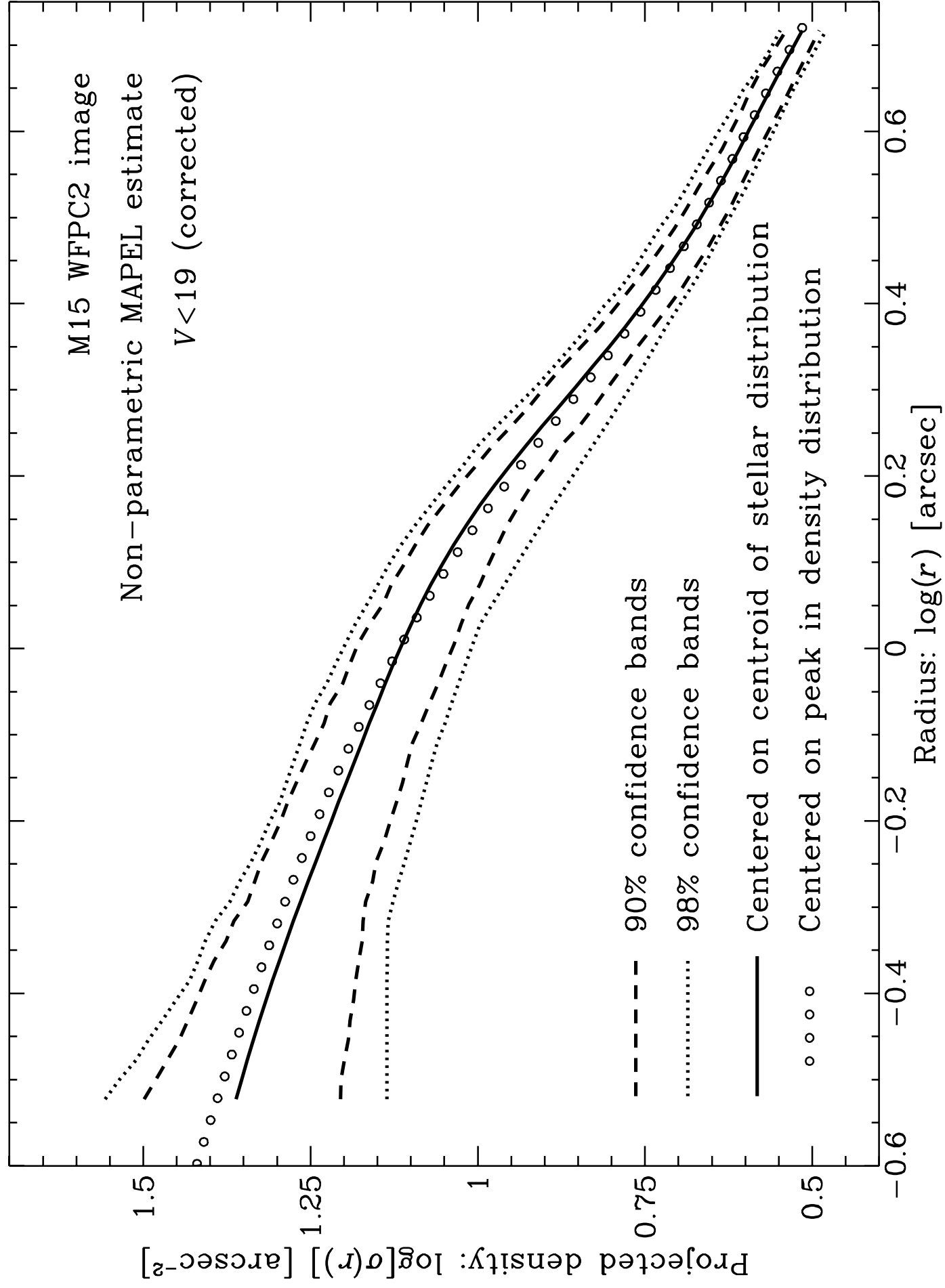


Fig. 12

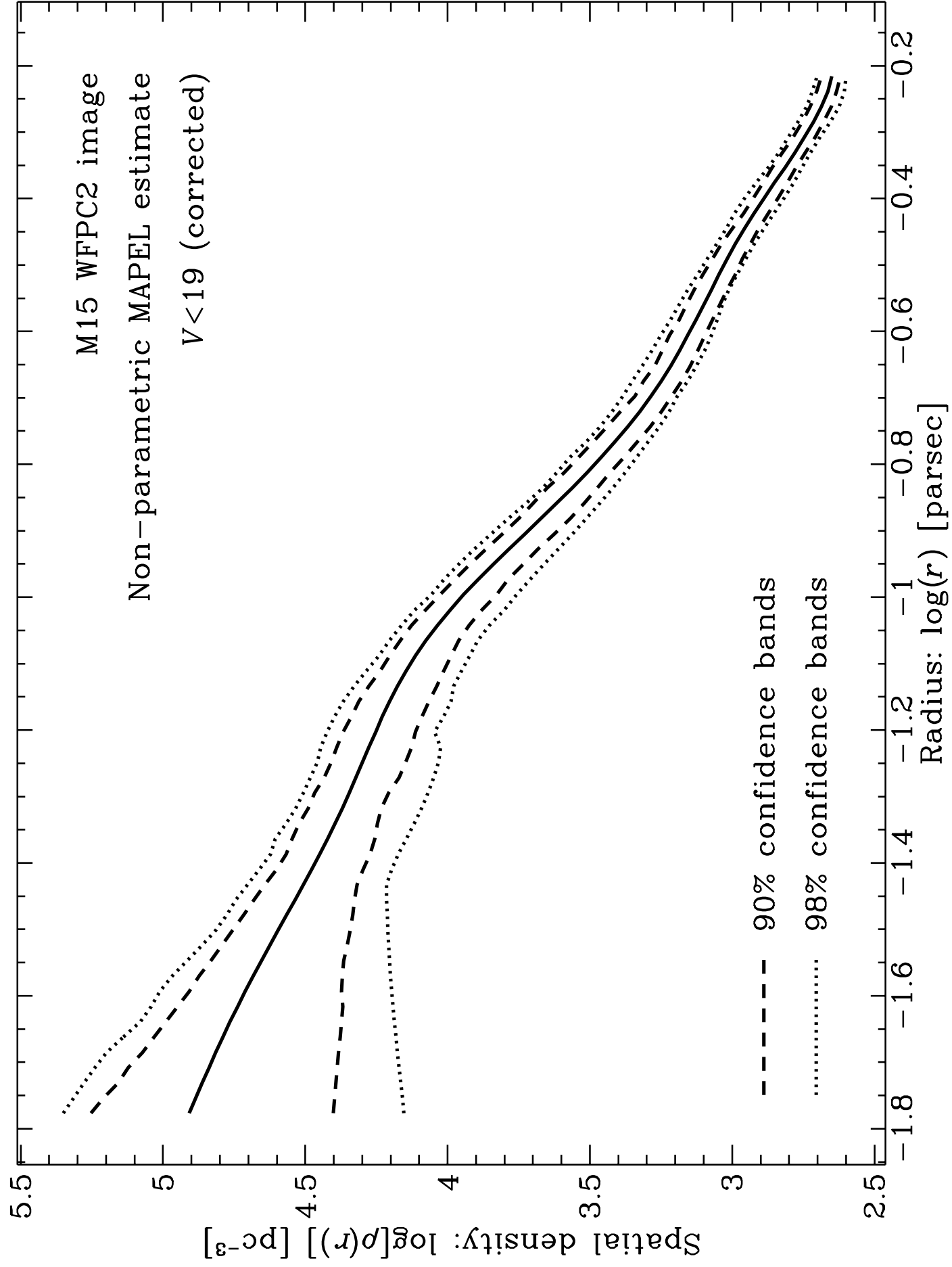


Fig. 13

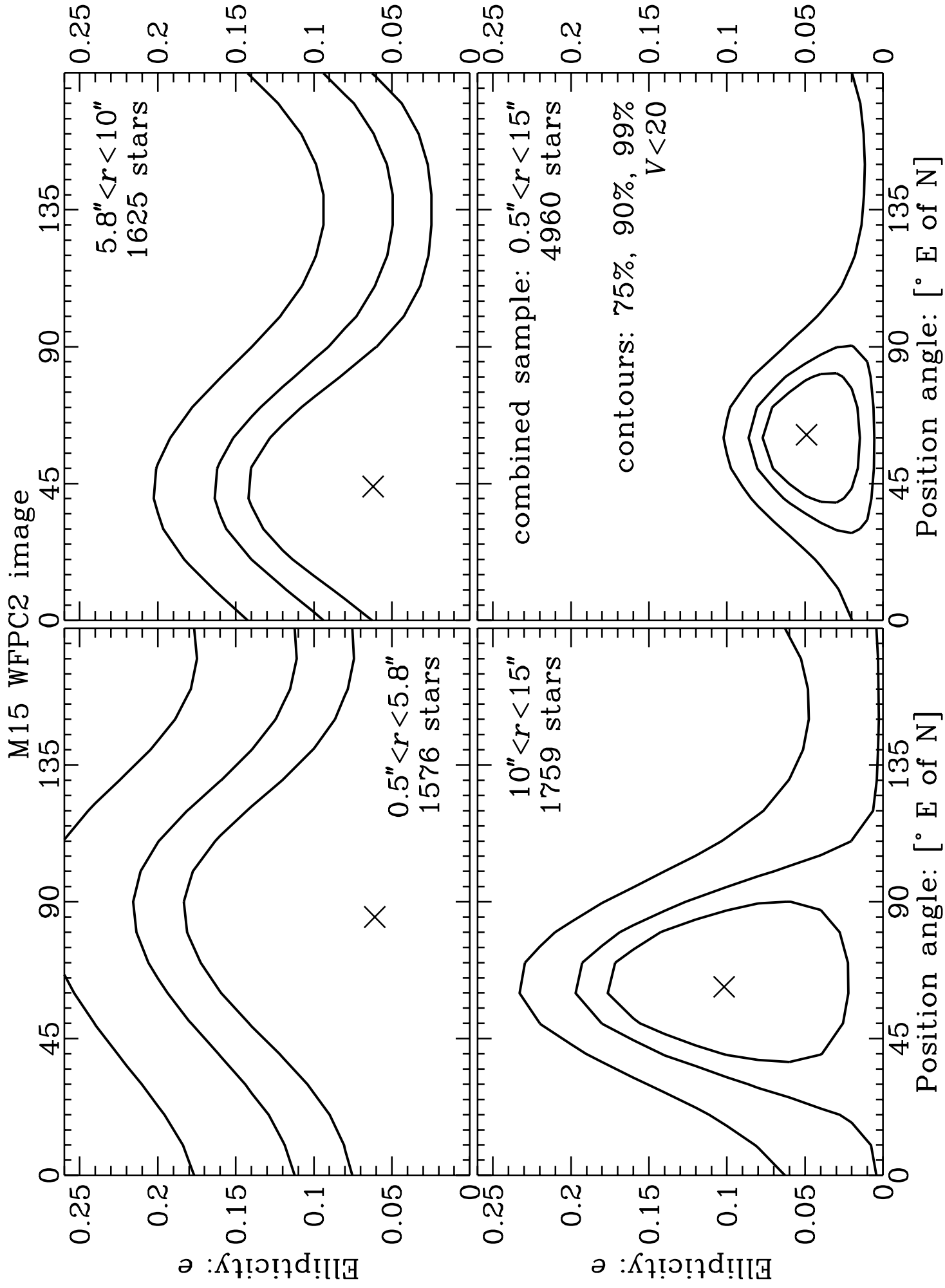


Fig. 14